Mon. Not. R. Astron. Soc. **000**, 1–12 (2011)   Printed 13 January 2013   (MN LaTeX style file v2.2)

arXiv:1102.4872v1 [astro-ph.GA] 23 Feb 2011

Atomic Hydrogen produced in M 33 Photodissociation Regions

J. S. Heiner[1,2,3]⋆, R. J. Allen[2] and P. C. van der Kruit[3]
[1] *Département de Physique, Université Laval, Québec, QC G1V 0A6, Canada*
[2] *Space Telescope Science Institute, Baltimore, MD 21218, USA*
[3] *Kapteyn Astronomical Institute, University of Groningen, PO Box 800, 9700 AV Groningen, the Netherlands*

Draft of 13 January 2013

ABSTRACT

We derive total (atomic + molecular) hydrogen densities in giant molecular clouds (GMCs) in the nearby spiral galaxy M 33 using a method that views the atomic hydrogen near regions of recent star formation as the product of photodissociation. Far-UV photons emanating from a nearby OB association produce a layer of atomic hydrogen on the surfaces of nearby GMCs. Our approach provides an estimate of the total hydrogen density in these GMCs from observations of the excess far-UV emission that reaches the GMC from the OB association, and the excess 21-cm radio Hi emission produced after these far-UV photons convert H_2 into Hi on the GMC surface. The method provides an alternative approach to the use of CO emission as a tracer of H_2 in GMCs, and is especially sensitive to a range of density well below the critical density for CO(1-0) emission.

We describe our "PDR method" in more detail and apply it using GALEX far-UV and VLA 21-cm radio data to obtain volume densities in a selection of GMCs in the nearby spiral galaxy M 33. We have also examined the sensitivity of the method to the linear resolution of the observations used; the results obtained at 20 pc are similar to those for the larger set of data at 80 pc resolution. The cloud densities we derive range from 1 to 500 cm^{-3}, with no clear dependence on galactocentric radius; these results are generally similar to those obtained earlier in M 81, M 83, and M 101 using the same method.

Key words: galaxies: individual (M 33) - galaxies: ISM - ISM: clouds - ISM: molecules - Ultraviolet: galaxies - ISM: atoms

1 INTRODUCTION

Molecular hydrogen is the major component of baryonic matter in the Universe, but direct observations of its large-scale distribution and motions within and between galaxies are hampered by the fact that the molecule has no dipole moment. The absorption and emission of radiation from H_2 can occur via the much weaker quadrupole coupling, but the lowest rotational transition has $E/k = 510\mathrm{K}$ ($\lambda = 28.2\mu$) and emission therefore requires a significant heat source for excitation. Secondary tracers of H_2 include the rotational lines of the CO molecule and infrared continuum emission from the accompanying dust, but the excitation requirements of the former favor gas at relatively high density ($n \gtrsim 1000$ cm^{-3}) and the thermal radiation properties of the latter favor gas at relatively high temperature ($T_K \gtrsim 20$ K) and depend on grain characteristics. The cool ($\lesssim 10$K), sparse ($n \lesssim 100$ cm^{-3}) component of the ISM occupies a region of parameter space that is difficult to explore, and its contribution to the total gas content of a galaxy remains uncertain.

In nearby galaxies, the most common indirect means of detecting molecular hydrogen is carbon monoxide (CO), tracing dense, relatively cold molecular gas. On galaxy-wide scales, CO may or may not be a good indicator of the total molecular gas content, but on the scale of individual complexes of giant molecular clouds (GMCs) the situation becomes more complicated. See, for example, Leroy et al. (2007) and Leroy et al. (2009) on CO-free H_2 envelopes in the Small Magellanic Cloud. Langer et al. (2010) present recent observations of [CII] emission without CO counterparts, tracing warm H_2 gas.

Another way to trace the 'total gas' is through infrared dust emission (Israel 1997). Recent results from *Herschel* have greatly expanded the potential application of this approach (e.g. Braine et al. 2010).

⋆ E-mail: jonathan.heiner.1@ulaval.ca

Here we use an alternative method that is sensitive to low-density gas, and is relatively insensitive to temperature. The tracer is atomic hydrogen, considered to be a result of photodissociation of H_2 by far-uv photons emanating from OB associations of young massive stars and impinging on the surfaces of nearby giant molecular clouds (GMCs). A simple model of the photodissociation process in these photodissociation regions (PDRs) permits us to estimate the total volume density (atomic + molecular) of the GMC as a function of its relative dust content, the intensity of the incident far-UV radiation, and the column density of the HI created on the cloud surface. Observations of nearby galaxies by the GALEX satellite provide the far-UV data, the VLA radio telescope provides HI column densities from 21-cm emission, and optical emission lines in the ionized gas near the OB association provide estimates of the local dust/gas ratio. Allen et al. (1986) presented the first evidence that dissociation of H_2 into HI occurs on kiloparsec scales in the nearby galaxy M 83, and in the meantime several nearby galaxies have been studied in more detail including M 81 (Allen et al. 1997; Heiner et al. 2008a), M 101 (Smith et al. 2000), and (again) M 83 Heiner et al. (2008b). We will refer to this approach as the "PDR method", which we describe and apply here to M 33.

The nearby galaxy M 33 is an obvious choice to apply the PDR method to and derive total hydrogen volume densities from it. M 33 is close enough to permit resolving some of the atomic hydrogen structures around sites of recent star formation. Besides utilizing the full resolution available in the FUV and HI images (≈ 20pc), we also apply the method at a deliberately reduced resolution (≈ 80pc), which has the advantage of revealing more of the larger scale structure of the PDRs and allows us to compare the M 33 results to our previous M 81 and M 83 results. The latter two galaxies are at a distance of 3.6 and 4.5 Mpc respectively, but M 33 is considerably closer, at 847 kpc (Saha et al. 2006), and therefore offers a superior linear resolution at the same angular resolution. At the same time M 33 is not too close to lose the larger-scale morphology, while being reasonably face-on. The influence of resolution effects on the PDR method can also be studied this way.

Recent work on M 33 has revealed the detailed distribution of molecular clouds detectable in CO emission (e.g. Onodera et al. 2010; Gratier et al. 2010; Rosolowsky et al. 2007). Metallicities in M 33 have been investigated with increasing spatial resolution (Rosolowsky and Simon 2008; Magrini et al. 2010), and Braine et al. (2010) treat the dust and gas this galaxy. To this expansive host of results, we add independent total hydrogen volume density measurements using the PDR method.

In Heiner et al. (2009) we presented the first results of applying the PDR method to M 33 at high resolution. In Heiner et al. (2010) we showed how the PDR method at reduced resolution can be used to measure the power-law slope of the volume Schmidt law of star formation as originally formulated by Schmidt (using volume density instead of surface density). In this paper we present our full PDR method results of M 33 that were used in the previous two papers, at high resolution as well as reduced resolution. The aim of this work is to compare the densities with our previous M 81 and M 83 results and test the consistency of the PDR method at two widely different linear resolutions.

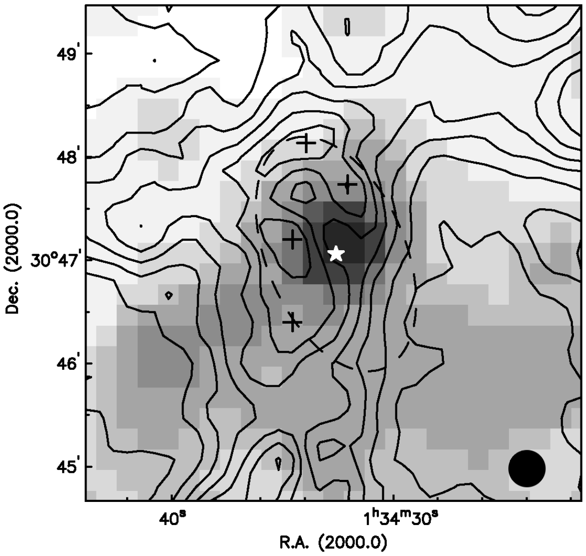

Figure 1. Example: NGC 604 seen as a large candidate PDR. Gray scale levels (FUV counts per second per pixel) are 0.25, 0.5, 0.75, 1, 2.5, 5, 7.5, 10, 25, 50. The fitted centre of the UV emission is marked with a white star. The HI contour levels are (in 10^{21} cm^{-2}) 0.5, 1, 1.5, 2, 2.5. Measured HI patches are indicated with black crosses. The dashed ellipse is an example of how ρ_{HI} was measured - namely de-projected using M 33's position angle and inclination. Its major axis has a radius of about 280 parsec. A 20-arcsec beam is drawn in the lower right.

The data used as input for the PDR method and the method itself are detailed in Section 2. The total hydrogen volume densities in candidate PDRs in M 33 are presented in the next section: the densities from the reduced resolution analysis in Section 3.2 and the full resolution results in Section 3.3. We briefly compare the results of the PDR method in M 33 to those in M 81 and M 83 and summarize our conclusions in Section 4.

2 DATA AND METHOD

2.1 The PDR method

Determining the total hydrogen volume density in candidate PDRs requires measurements of the local radiation field, which we estimate from FUV photometry derived from the publicly available *GALEX* M 33 image. It also requires identifying potential GMCs, traced by 'patches' of atomic hydrogen: distinct features of HI found near OB star clusters. We focus on FUV emission above the diffuse background radiation field and we assume that this emission causes the distinct HI features above the HI background levels. In this manner we attempt to obtain clear and simple components to our method and keep the geometry of the candidate PDRs surrounding the OB clusters simple.

The 21-cm 20-arcsec and 5-arcsec M 33 images were provided by David Thilker and Rob Braun (2007, private communication). The linear resolution for the reduced resolution comparison is about 80 pc at the distance of M 33, from a combination of data from the VLA (B, C and D configurations) and the GBT (for a complete explanation of the

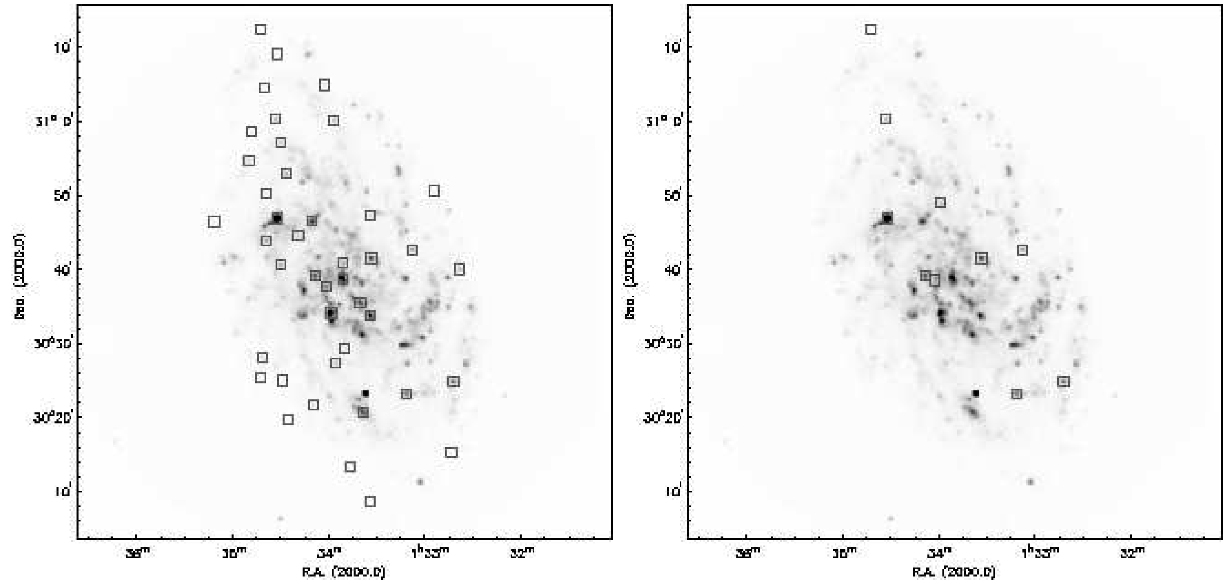

Figure 2. Candidate PDR locations are indicated with boxes on this *GALEX* FUV image (smoothed to 30-arcsec). The candidate PDRs were selected on the basis of their FUV emission. Left panel: reduced resolution regions. Right panel: full resolution regions.

Source no.	R.A. (2000)	Decl. (2000)	Radius (kpc)	F_{FUV} [a]	Aperture (arcsec)
1	1 33 51.371	30 38 52.01	0.23	305.35	96
2	1 33 51.052	30 41 1.18	0.40	26.08	36
3	1 33 40.271	30 35 34.72	1.16	137.22	72
4	1 34 1.540	30 37 43.83	1.27	71.03	60
5	1 34 8.658	30 39 15.42	1.63	96.25	72
6	1 33 34.135	30 33 53.24	1.71	151.01	72
7	1 33 33.401	30 41 37.88	1.88	188.70	156
8	1 33 58.709	30 34 14.98	1.92	518.50	156
9	1 34 10.340	30 46 39.52	2.06	195.81	108
10	1 34 19.129	30 44 37.26	2.35	20.08	48

[a] 10^{-15} ergs cm^{-2} s^{-1} Å^{-1}

Table 1. Locations and FUV fluxes of candidate PDRs (example, full table available in the ***(online version of this journal)***).

procedure, see Braun et al. 2009)[1], and the full resolution analysis was carried out at a 5-arcsec resolution. The images are a mosaic of radio pointings that cover the extent of the *GALEX* image. At the 5-arcsec resolution, typical noise levels are 2×10^{20}cm^{-2}.

To calculate linear distances within M 33, necessary to compute incident UV fluxes, we assume this galaxy to be located at a distance of 847 kpc (Saha et al. 2006). (The same parameters were used in Heiner et al. 2009). To de-project distances, we adopt a position angle of 23° and an inclination of 56° for its disc, from Zaritsky et al. (1989). Its R_{25} is 28.8′, or 7.1 kpc (Vila-Costas and Edmunds 1992), which we used to normalize our galactocentric radius measurements. The radius measurements are needed to calculate the dust-to-gas ratio with the assumption of a galactic metallicity gradient. A uniform foreground extinction of $A_{FUV} = 0.33$mag is assumed to correct the measured UV flux, using E(B-V) from Schlegel et al. (1998) and the expression for A_{FUV} from Gil de Paz et al. (2007). As in our previous papers, we ignore internal extinction, under the assumption that it is uniform, or at least acting in all directions equally in a spherical morphology, and that the distance through the disc is comparable to the separation between the UV source and the HI patch. In that idealized case the internal extinction can be ignored, as it works equally between the UV source and the observer as between the UV source and the HI patch. The adoption of a single value for the internal extinction affects the calculated values of the total hydrogen volume densities equally. For example, if an internal extinction of 1 mag were adopted, all values of n would need to be multiplied by 2.5. We also use the GALEX FUV emission at 1500Å as a proxy for the dissociating radiation at 1000Å, assuming a locally flat spectral energy distribution (van Dishoeck and Black 1988).

The photodissocation rate is regulated by the dust content, through obscuration of FUV radiation and catalyzation of the formation of molecular hydrogen. We derive the dust-to-gas ratio δ/δ_0, which is normalized to

---

[1] Project codes for the radio data: (VLA) AT206, AT268, and (GBT) GBT02A-038

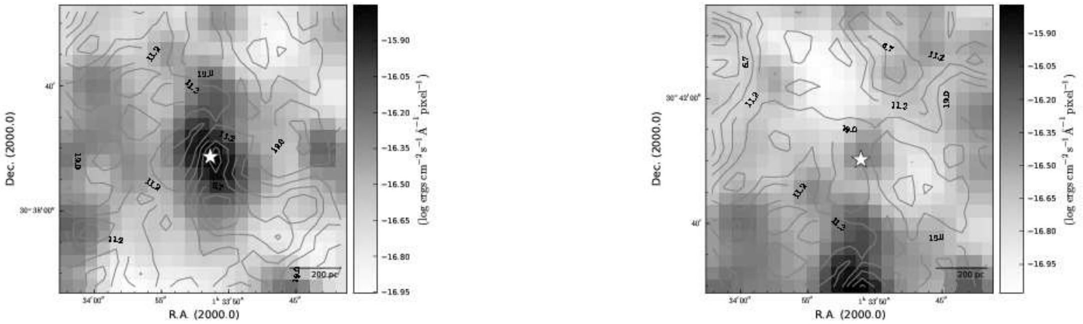

1 2

Figure 3. M 33 candidate PDRs at reduced resolution (the full set is available in the ***(online version of this journal)***). The H I column density contours are plotted against a background of the FUV flux in gray scale. The fitted position of the central UV complex is marked by a star. A distance scale is indicated, but see Figure 1 about how we de-project the distances. The integrated FUV fluxes can be found in Table 6.

Source no.	$\rho_{\rm HI}$ (pc)	$N_{\rm HI}$ (10^{21} cm^{-2})	G_0	G/G_{bg}	n (cm^{-3})	[a]
1a	121	1.91	6.53	8.01	487	0.60
1b	161	2.02	3.67	4.51	249	0.59
1c	403	2.17	0.59	0.72	35	0.58
2a	40	2.11	5.02	8.18	323	0.97
2b	202	2.37	0.20	0.33	10	0.61
2c	363	1.57	0.06	0.10	6	0.52
2d	363	2.17	0.06	0.10	4	0.58
3a	242	1.82	0.73	0.81	67	0.54
3b	242	1.51	0.73	0.81	89	0.51
3c	403	1.99	0.26	0.29	21	0.55

[a] Fractional error

Table 2. Results (example, full table available in the ***(online version of this journal)***).

the solar neighborhood value, from the metallicity 12 + log(O/H) after Issa et al. (1990). Under this assumption, the dust-to-gas ratio is directly proportional to the metallicity log(O/H). The metallicities in M 33 were measured by Rosolowsky and Simon (2008) and Magrini et al. (2007). We use a solar metallicity of 8.69 from Allende Prieto et al. (2001) to obtain the dust-to-gas ratio scaled to the solar neighborhood. The dependence of the dust-to-gas ratio on the galactocentric radios R (in kpc) is:

$$\log \delta/\delta_0 = -0.027R - 0.33, \tag{1}$$

using Rosolowsky and Simon (2008). More recently, Magrini et al. (2010) report a metallicity slope of 0.037 dex kpc^{-1}. However, we will keep the slope of 0.027 for consistency with our previous results.

With the full resolution data local metallicity measurements are sometimes available for our candidate PDRs; in these cases we adopt an equivalent expression to that used in Heiner et al. (2009), independent of the galactocentric radius:

$$\log \delta/\delta_0 = (12 + \log{(O/H)}) - 8.69. \tag{2}$$

The foreground extinction that was used to correct the far-UV flux is 0.33 mag, based on Schlegel et al. (1998) and Gil de Paz et al. (2007). The equation describing the photodissociation process, as derived from Sternberg (1988) and Allen (2004) is:

$$N_{\rm HI} = \frac{7.8\times10^{20}}{\delta/\delta_0} \ln\left[1 + \frac{106G_0}{n}\left(\frac{\delta}{\delta_0}\right)^{-1/2}\right] \ {\rm cm}^{-2}. \tag{3}$$

In this form it is a clear expression of the atomic hydrogen column density that is created by photodissociation on the surface of GMCs.

Heaton (2009) derived a somewhat improved version of this equation, requiring all derived values of n in this paper to be multiplied by $(\delta/\delta_0)^{0.2}$, which is well within our current estimated levels of uncertainty in the case of M 33. We maintain the use of Equation 3 at this time for consistency with our results in Heiner et al. (2009) and Heiner et al. (2010).

We considered the overall H I distribution across the disc of M 33 and adopted a background H I column density of 1.2×10^{20} cm^{-2} inside 1.1 R_{25} and 0.5×10^{20} cm^{-2} outside of this radius. We do this in an attempt to isolate the additional H I produced by photodissociation under the influence of the nearby OB associations. We checked the reduced resolution background levels of the H I column densities throughout M33 and chose to characterize the trend with these two values. They have a very small impact on the final results as long as they are only a fraction of the 7.8×10^{20} scaling in the exponential of the model when computing the total hydrogen volume density n. We measured the distances between the central UV source and nearby H I 'patches', which are defined as a local maximum in the H I column density, and recorded their column densities out to a separation of 400 pc, the approximate maximum size of the candidate PDRs.

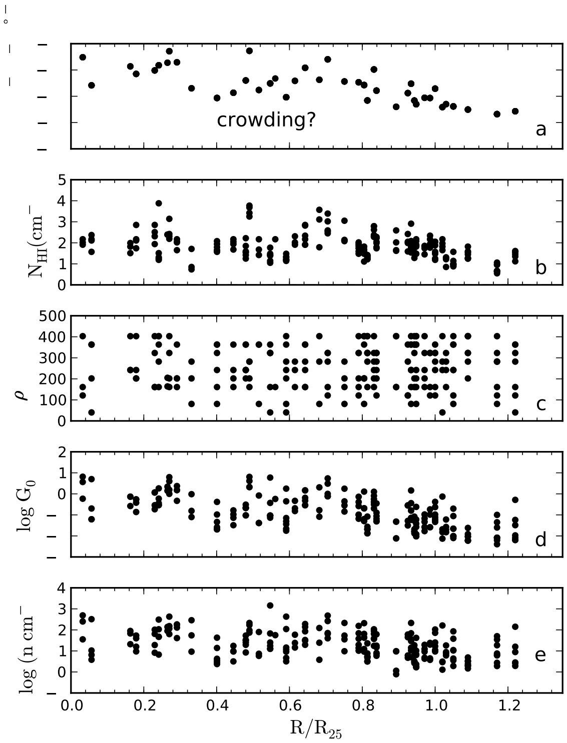

Figure 4. Combined results are plotted here as a function of the normalized galactocentric radius. (a) FUV fluxes of the candidate PDRs, not corrected for extinction. (b) HI column densities associated with the central UV sources. (c) ρ_{HI}, the separation between the central UV source and each HI patch. (d) Incident flux G_0 on each HI patch. (e) Total hydrogen volume densities $n = n_{\mathrm{HI}} + 2n_{\mathrm{H_2}}$.

This value is somewhat arbitrary and based on the HI morphology surrounding the central UV source. In Heiner et al. (2008a) we used 600 pc, although almost all measured values were below 400 pc. In Heiner et al. (2008b) we used 480 pc. Erroneously including HI patches that are not produced under the influence of the assumed central UV source results in low computed total hydrogen volume densities.

We censored background-subtracted column densities below 0.5×10^{20} cm^{-2}. As an example of the resolution of the data and the scale of the candidate PDRs, we show NGC 604 in Figure 1. The HI contours illustrate the morphology of atomic hydrogen surrounding the central concentration of O and B stars in NGC 604, the brightest HII region in M 33. While this region has been studied in much more detail (at a much higher resolution), it is important in the context of large-scale PDRs to view this region in its entirety and to get global gas density estimates from it. In the full resolution HI data we measured individual local HI column density backgrounds based on the average HI column density near the candidate PDRs. These background levels will be listed for every region in the full resolution results.

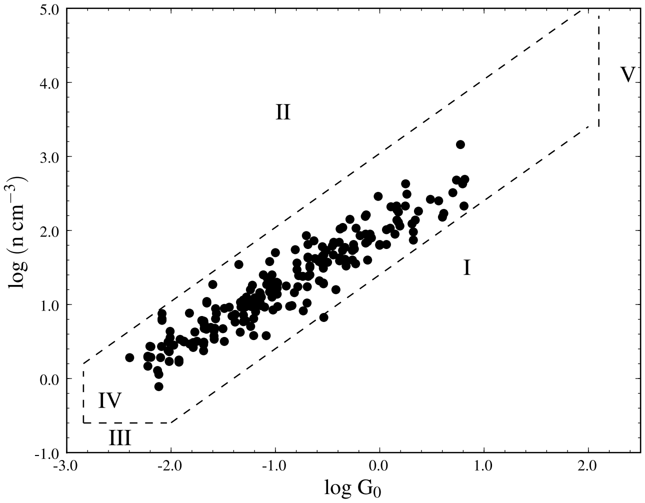

Figure 5. Observational limits are marked in this plot of G_0 versus n. The roman numerals are explained in the text.

Name	Reduced resolution no.
CPSDP Z204	5
CPSDP 0087g	near 5
BCLMP 0695	none
BCLMP 0650	24
BCLMP 0288	19
BCLMP 0269	27
NGC 604	14
NGC 595	7
BCLMP 0256	20
Region 42	42

Table 3. Candidate PDRs, full resolution

2.2 Improvements to the PDR method

The full resolution images allow for a slight improvement to the PDR method. Resolved UV sources are measured independently (although they are still expected to harbor a certain amount of O, B stars each) and their incident flux G_0 on individual HI patches is summed to derive a cumulative G_0. We did not consider whether one UV source blocks another in the direction of an HI patch, since we could not de-project the three dimensional structure of these OB clusters from the FUV image. It can however be assumed that this is not a big issue if the extinction close to these sources is low.

Another improvement to the method is the use of locally measured metallicity values where available (Equation 2). Otherwise, we use the single metallicity gradient equation for M 33 (Equation 1). As in M 81 and M 83, we did not aim for a complete sample of candidate PDRs in M 33, but rather we selected those regions that stood out in their FUV emission and had a morphology that seemed to indicate the presence of large-scale PDRs. The latter merely means that we preferred regions with a relatively simple apparent HI morphology. We selected regions with a progressively more (apparent) complex HI structure. Additionally, when a larger, resolved HI structure appeared to be present in a candidate PDR, we measured its average column density and calculated a global total hydrogen volume density. This is similar to the method used in M 81 and M 83, except that in M 33 the structures are resolved. We explicitly assume that a large-scale PDR with a shell of HI is observed in these cases, with a radius of up to a few hundred parsec. NGC 595 is an example where this morphology is particularly obvious.

In addition to the UV-selected candidate PDRs, we included a few regions that had either individual CO detections associated to it, from Engargiola et al. (2003), or individual metallicity measurements. Almost all of these candidate PDRs, primarily selected by FUV emission, are previously catalogued HII regions. The ones starting with BCLMP derive their names from Boulesteix et al. (1974). The ones starting with CPSDP come from Courtes et al. (1987). Our sample includes one region that has no name at this time, which we will call "Region 42", consistent with the numbering of the reduced resolution results.

3 RESULTS

3.1 Source selection

The candidate PDRs that were selected for our analysis are shown in Figure 2. We selected 42 prominent FUV sources in M 33 at reduced resolution, while attempting to cover the full range of galactocentric radii available to us. Each UV-selected region has multiple measured HI patches, providing a range of total hydrogen volume density measurements per candidate PDR. Note that we did not aim to identify all candidate PDRs, as source completeness was not our goal.

At the full resolution, we selected 10 regions. At this level of detail, the larger scale (a few hundred parsec) morphology of HI is resolved into smaller scale (several tens of parsec) HI features. It is important to see if the results of the PDR method change when applying it at full resolution. We also wanted to take advantage of the availability of individual dust-to-gas ratio measurements. Finally, some regions also had measurements of CO available, so the resulting cloud densities can be compared to CO results. At the same time, we tried to preserve the spread in galactocentric radius coverage.

The full resolution HI morphology is considerably more detailed, and identifying clear HI patches is not easy as in the reduced resolution case. Therefore, we selected a limited subset of the regions featured in the reduced resolution analysis and studied them more extensively. Table 3 shows how the selected regions correspond to the reduced resolution regions. The full resolution regions are chosen with several criteria in mind: apparent presence of a large scale HI (partial) shell, known HII regions (e.g. NGC 604), availability of individual metallicity data, and availability of CO measurements, while still keeping a representative spread in galactocentric radius. The final sample included 10 regions. 8 of these are also present in the reduced resolution sample, one is an HII region close to a reduced resolution region and one does not appear in the reduced resolution analysis. These 10 regions feature a rich and detailed morphology, while at the same time the resulting total hydrogen volume densities are shown not to differ significantly from the reduced resolution analysis result. (See Section 4.1.)

3.2 Cloud densities in M 33, reduced density

Two example overlays of M 33 candidate PDRs (locations are marked in Figure 2) at reduced resolution are shown in Figure 3. A full set of overlay plots can be found in the ***(online version of this journal)***.

The FUV fluxes of the central sources in our candidate PDRs are displayed in Figure 4a, and listed in Table 1 along with their locations and the aperture used to measure the FUV flux and the galactocentric radius of each source.

A gradual decline in maximum values can be seen going outwards. A similar decline can be seen in the minimum values, but we suspect that crowding effects are possible here, leading us to miss the fainter sources. We are assuming that the maximum values are real and not a selection effect, whereas a sensitivity limit has been reached at larger galactocentric radius. The fluxes show the same spread as we reported for M 83 (Heiner et al. 2008b) - namely 2 dex or less at any given galactocentric radius. Since associations of O and B stars are measured, the number of those stars per cluster could decrease with radius, causing the general decline. On an absolute scale the difference in flux values is caused only by the different distances of M 83 and M 33 (the luminosities of the UV sources are in the same range).

The measurements of the candidate PDRs are shown in Figure 4 and in Table 2. The figure and table show the measured HI column densities of candidate PDRs, the separation between the OB clusters and associated HI patches, the calculated incident flux G_0,and finally the derived total hydrogen volume densities.

Figure 4b shows the HI column densities of the patches found near each of the UV sources. The patches are local maxima in the column densities that are assumed to be caused by HI produced in a PDR. Each UV source can have multiple HI patches associated to it. The measured HI columns are fairly flat out to a radius of 0.8 R_{25} (with some spread), after which they start to decline. The maximum measured column densities are affected by beam smoothing and related to the linear resolution.

Using the measured separation between the central UV source in each candidate PDR and its associated HI patches ($\rho_{\rm HI}$, Figure 4c), the incident flux G_0 on every patch is calculated, and plotted in Figure 4d. The distribution of G_0 values is mostly flat out to a radius of 0.8 R_{25}, and after that the values start to decline due to the decreasing measured FUV fluxes. The distribution of measured separations $\rho_{\rm HI}$ does not change with galactocentric radius and shows no preferred value.

Finally we calculate the total hydrogen volume densities n, which are plotted in Figure 4e, using Equation 3. Values range from 1 to 500 cm^{-3} with values going up to 2500 cm^{-3} and do not change significantly with galactocentric radius. This corresponds to H_2 densities of up to 250 cm^{-3} in GMCs across M 33. A hint of an upturn at large galactocentric radius may be caused by overestimating the dust content and is not significant.

It is also instructive to plot the relation between G_0 and n, as displayed in Figure 5, because of the selection effects, marked by dashed lines:

I. HI column density upper limit of 5×10^{21} cm^{-2} at a characteristic δ/δ_0 of 0.33.

II. HI column density lower limit of 6×10^{19} cm^{-2} at a

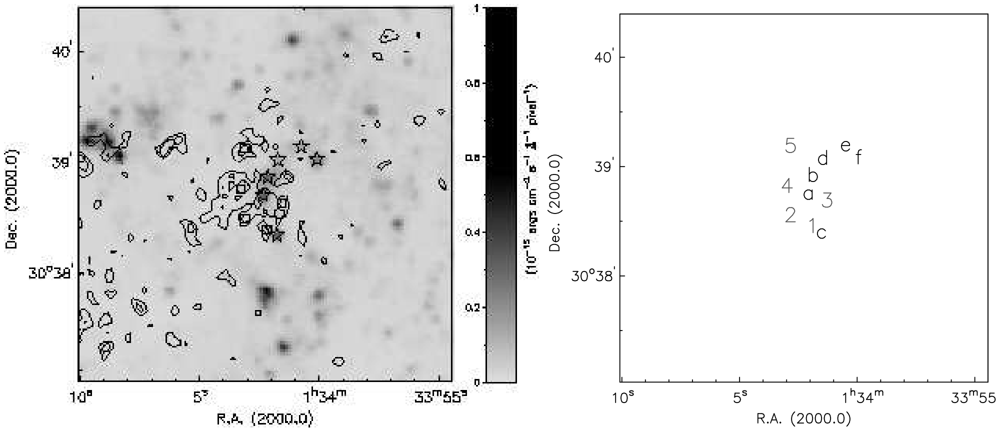

Figure 6. Left panel: CPSDP 0087g region at full resolution. The FUV image is overlaid with HI contours (color version available in the ***(online version of this journal)***. The HI contours are 3 and 4 $\times 10^{21}$cm^{-2} only, to emphasize the morphology of the HI peaks. Black stars mark the locations where the FUV fluxes were measured. The orange boxes are the locations of the measured HI patches. Green diamonds denote the location of CO detections by Engargiola et al. (2003). Part of CPSDP Z204 can be seen in the eastern part of the image. Right panel: Finding chart of the same region with letters (UV sources) and numbers (HI patches).

R_{gal} (kpc)	1.05
δ/δ_0	0.65
FUV sources (J2000)	$1^h34^m2.363^s$ $30°38'42.30''^a$, $1^h34^m2.175^s$ $30°38'52.13''^b$, $1^h34^m1.792^s$ $30°38'20.99''^c$, $1^h34^m1.754^s$ $30°39'01.48''^d$, $1^h34^m0.781^s$ $30°39'08.93''^e$, $1^h34^m0.127^s$ $30°39'01.85''^f$
FUV fluxes (10^{-15} ergs cm^{-2} s^{-1} Å^{-1})	4.55^a, 4.68^b, 4.55^c, 1.56^d, 1.65^e, 4.72^f
$N_{bg}(10^{21}$ cm$^{-2})$	0.96
$N_{HI}(10^{21}$ cm$^{-2})$	$3.37^{1:abcd}$, $4.10^{2:abc}$, $3.67^{3:abcdef}$, $4.63^{4:abcd}$, $3.64^{5:abcd}$
G_0 (cumulative)	1.69^1, 0.32^2, 0.97^3, 0.48^4, 0.37^5
G/G_{bg} range	$0.01-1.77^1$, $0.03-0.17^2$, $0.01-0.23^3$, $0.01-0.16^4$, $0.02-0.09^5$
n (derived, in cm^{-3})	15^1, 1^2, 6^3, 1^4, 3^5
Fractional error range	$0.35-0.45$

Table 4. Detailed measurements of CPSDP 0087g

characteristic δ/δ_0 of 0.25. Note however that this lower limit can be higher in practice, as it also depends on our ability to discern HI patches against the general HI background.

III. Lowest observable n of 0.2 cm^{-3} related to the radio beam size and the HI lower limit.

IV. Minimum usable G_0 of 1.4×10^{-3}, depending on the maximum accepted size of candidate PDRs and the lowest accepted UV flux.

V. Maximum G_0 obtainable by the PDR method considering our data of M 33 of 1.2×10^2.

Clearly, the selection effects limit the possible values of G_0 and n.

3.3 Cloud densities in M 33, full resolution

We will now present the cloud densities in candidate PDRs as derived with the PDR method from the full resolution (~ 20 pc linear resolution) data. These are mostly a subset of the regions selected for the reduced resolution analysis. The corresponding regions are listed in Table 3. We will give a short description of each region, accompanied by an overlay plot, a finding chart and a data table. The color plots, finding charts and data tables are available in ***(the online version of this journal)***. An example plot, finding chart and table are shown for CPSDP 0087g in Figure 6 and Table 4. The results for the regions NGC 604 and CPSDP Z204 are included for completeness, but were presented previously in Heiner et al. (2009). Finally, the results are gathered in a couple of consolidated plots. An overview plot of the location of the regions that were investigated is shown in Figure 2.

CPSDP 0087g: We measured fluxes in a string of UV sources, that seems to be surrounded by HI emission. (Figure 16, Table 7.) The HI morphology is clumpy and is mostly located to the east of the UV sources. This region has CO detections, that are not directly coinciding with measured HI patches. CO detection close to one of the UV sources is likely to arise from high temperatures. The metallicity in this region is relatively high, higher than, for example,

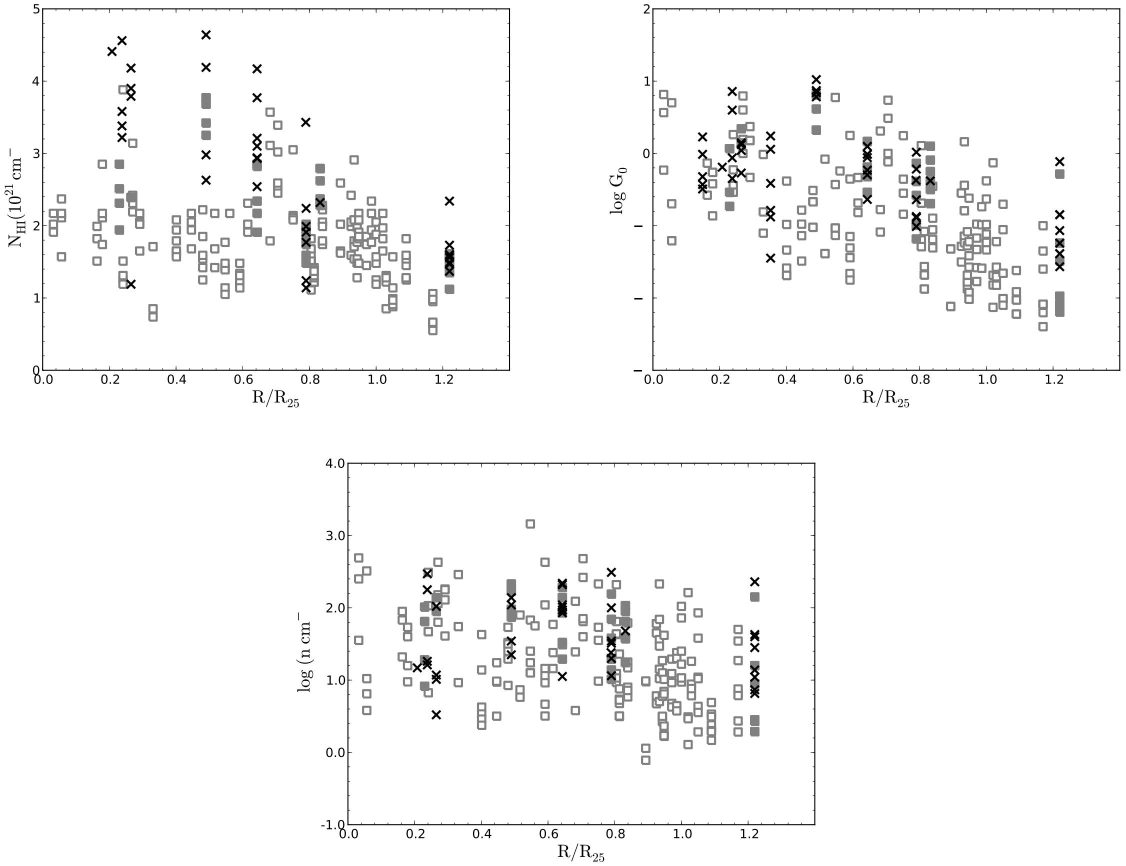

Figure 7. The results of the 9 out of 10 candidate PDRs that have detailed results (not the larger scale measurements) are shown here (as crosses): the HI column densities, the incident flux G_0, and the total hydrogen volume densities. The reduced resolution results are plotted as gray boxes. The filled boxes are the regions with full resolution result counterparts. Region BCLMP 0288 is not included since it does not feature a discernible detailed morphology.

CPSDP Z204 nearby. This depresses the total hydrogen volume densities in the PDR model.

CPSDP Z204 is about 1.6 kpc away from the centre of M 33 and is shown in Figure 17 and Table 8. It was described in more detail in Heiner et al. (2009) and shows a morphology of HI patches surrounding a complex of UV sources, making these HI clumps candidate PDRs. The detection of CO is a further confirmation of the presence of GMCs in the area.

NGC 595 is M 33's second brightest HII regions and has been studied extensively. Wilson and Scoville (1992) studied the molecular content of this region and found it to have less molecular gas mass than NGC 604 by about an order of magnitude (half a million solar masses). They noted a significant atomic mass component and point to photodissociation as the likely cause of this HI. Lagrois and Joncas (2009) derive an overal electron density of the nebula of 162 cm^{-3} from Hα, [O III] and [S II] kinematic observations. The finding chart in Figure 18 shows that HI patch no. 1, that was selected because it has CO associated to it, has a density of 105 cm^{-3} (Table 9). However, patch no. 2 is associated with CO emission as well, but has a lower density (only 12 cm^{-3}). The CO emission here may be the result of a higher temperature of the gas rather than a higher density of the GMCs. A larger scale measurements (green polygon in the overlay), yields a slightly higher density of 45 cm^{-3}.

BCLMP 0695: No clear large-scale structure can be discerned in this HII region, although the distribution of atomic hydrogen seems to suggest some filamentary structures. The UV fluxes are comparable to the lower fluxes in NGC 595, and the number of sources points to a lot of recent star formation (Figure 19). The UV sources surround the single detection of CO in this region, and so do the HI patches. The closest ones are no. 1 (23 cm^{-3}) and no. 4 (116 cm^{-3}). We would also expect CO emission at no. 2, since it has a density of 195 cm^{-3}, but it is also close enough to the UV source that any CO would have been broken up. In that case it would be of interest to look for ionized carbon atoms.

NGC 604 is the largest and most luminous HII region in M 33. Our measurements of NGC 604 are listed in Table 11. A detailed view of NGC 604 is shown in Figure 20. The central cluster of OB stars is situated on the edge of an HI arm. We attempted to get a global measurement using an average HI column density measured on the HI arm. HI column densities to the west of NGC 604 drop to below the sensitivity limit, although a diffuse component shows on single dish GBT data (Thilker, 2008, private communication).

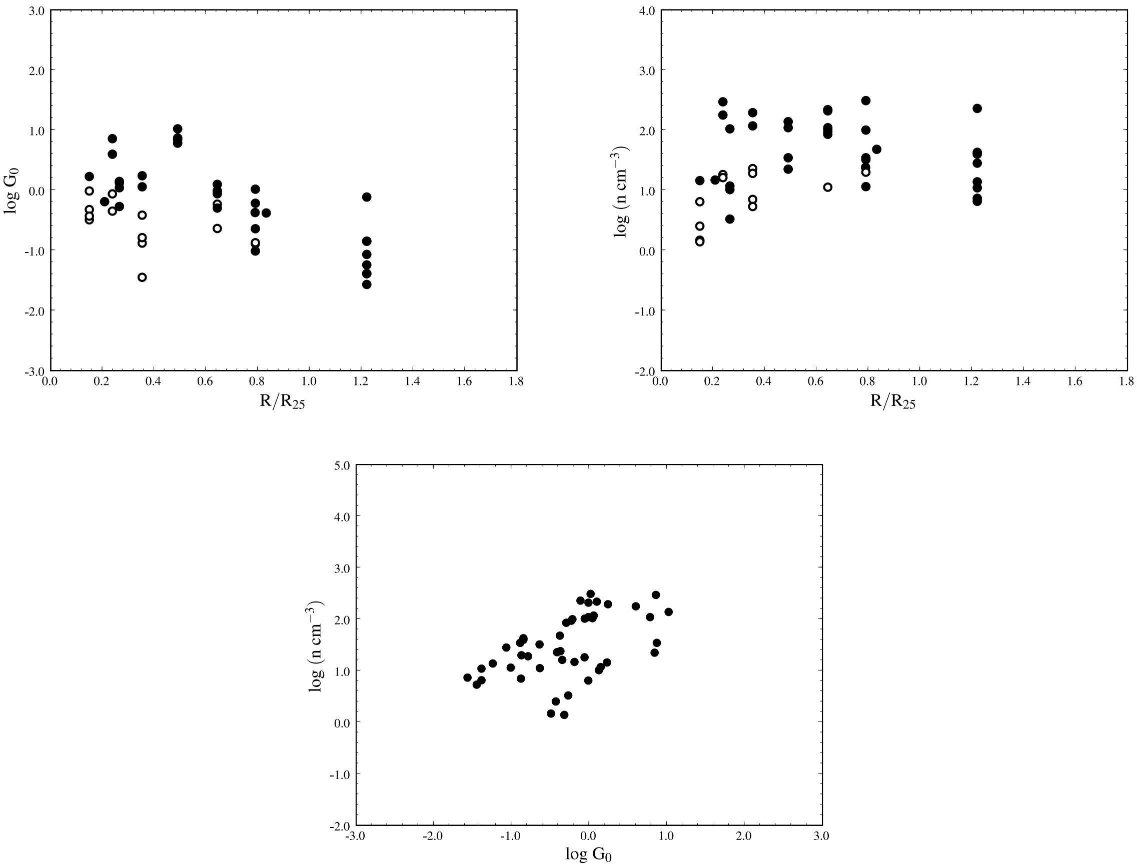

Figure 8. The results of the 9 out of 10 regions that have detailed results (not the larger scale measurements) are shown here: the incident flux G_0, the total hydrogen volume densities and a plot of n vs. G_0. The open circles indicate H I patches with a source contrast below 0.5. Region BCLMP 0288 is not included since it does not feature a discernible detailed morphology.

Since the UV emission does not particularly follow the H I arm, this faint H I emission deserves further attention.

Region BCLMP 0288 only features a morphology that suggests a large-scale PDR, which makes it an interesting target in its own right. The central cluster is embedded in H I emission that doesn't show discernible structure on a smaller scale. The highest H I columns go around BCLMP 0228 on the eastern side and we used an average along that ridge for our measurements (Figure 21, Table 12).

BCLMP 0256: This H II region contains three individual metallicity measurements from Rosolowsky and Simon (2008). We adopted the nearest measurement to each H I patch, as can be seen in Table 13. A partial H I ridge surrounding BCLMP 0256 on the basis of surrounding H I patches is shown, among others, in Figure 22. Additional UV sources were measured towards the west, where the extra metallicity measurements were available.

The region BCLMP 0650 (Figure 23) shows a rich morphology of a large-scale PDR and intermediate size PDRs, of which we have analysed 5. While the large-scale H I shell is not very dominant, we still attempted to measure its average column density in a rectangular area, finding a total hydrogen density of 18 cm^{-3}.

BCLMP 0269: This region features a lot of recent star formation, scattered over a relatively large area. The distribution of the atomic hydrogen surrounding the young star clusters is reminiscent of a large-scale shell. The average H I column density of this shell is measured along a straight line in Figure 24). The region includes a CO measurement by Rosolowsky et al. (2003), that we connect to an intermediate size PDR. We also include a similarly sized PDR on the eastern part of BCLMP 0269, which looks like our typical candidate PDR.

Our Region 42 lies relatively far from the centre of M 33, at about 8.6 kpc (Figure 25, Table 16). It features a single UV complex at its centre, surrounded by various H I patches that can be used to probe the underlying GMCs in this candidate PDR. These patches are expected to indicate medium scale PDRs. The total hydrogen volume densities found in this way range from 6 cm^{-3} to about 220 cm^{-3}. Additionally, we attempted to probe the large-scale PDR by averaging the H I column densities along an arc of H I surrounding the central FUV source. This measurements yields a total hydrogen volume density of n = 70 cm^{-3}. As in M 81 and M 83, our method points to the presence of GMCs in the outer regions of these galaxies.

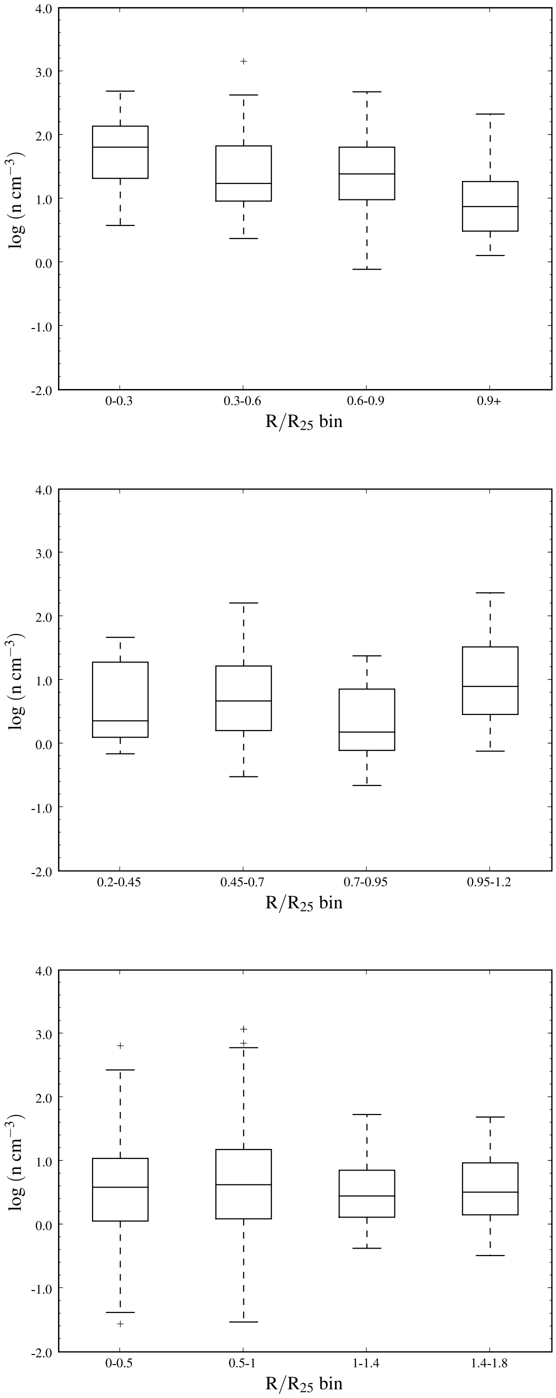

Figure 9. Boxplots showing the range of total hydrogen volume densities in the galaxies M 33, M 81 and M 83 respectively (from left to right). The bins have been chosen per galaxy to divide the available range of galactocentric radii in four parts. The M 83 results, previously published in Heiner et al. (2008b), show a greater spread in values within R_{25} than the other results. The M 33 results are narrower in spread and tend to be higher in total hydrogen volume densities.

3.4 Combined plots

The measurements of the regions with candidate PDRs presented here are consolidated in Figure 7. The results at full resolution are indicated with black crosses. The gray boxes in the background are the results at reduced resolution for reference. The filled boxes correspond to the regions investigated at full resolution. Note that one of the regions, BCLMP 0288, is not included since we only have a larger-scale measurement there (see Section 3.3).

The HI plot is a sampling of HI peaks that decline with galactocentric radius. Close to the centre of M 33 the values are high enough to raise worries about the HI being optically thick. The values of G_0 decline as well and generally span a range of 0.1 to 10. The total hydrogen volume densities are remarkably constant in range and values, ranging from approximately 10 to 300 cm^{-3}. The values in the region closest to the centre, CPSDP 0087g, are lower. We noted previously that this region has a particularly high dust content, depressing the densities that we obtain. The high dust content may also indicate heavy internal extinction for which we did not correct.

As an additional indication of the likelihood of the HI patches being produced by photodissociation, we looked at the source contrast G/G_{bg}. The same results are plotted without the reduced resolution results in the background. The open circles in Figure 8 indicate a corresponding source contrast of less than 0.5. These HI patches generally correspond to a lower value of n, and a lower value of G_0. Finally, plotting G_0 and n does not show a clear correlation, although if an actual correlation were present, it would be more pronounced without the CPSDP 0087g sources.

4 DISCUSSION AND CONCLUSIONS

4.1 Resolution effects

Despite the analysis at different resolutions, the resulting cloud densities do not differ from each other, as they are in the same range. This is shown in Figure 7, where the densities are shown for those regions that are included at both resolutions. The full resolution data offers the advantage of (partially) resolving the parent GMCs connected to the OB associations with the opportunity to study the behavior of the HI in more detail (Heiner et al. 2009). On the other hand, there is more confusion in the distribution of the HI, where the spatial distribution at the reduced resolution makes it easier to identify the HI patches. With the reduced resolution data presented here, we were able to study the volume Schmidt Law of star formation Heiner et al. (2009).

Either way, the resulting cloud densities do not differ significantly, and selecting more regions for full resolution study is not expected to lead to more insight at this time.

4.2 Performance of the PDR method across M 33, M 81, M 83

The M 81 and M 83 results were presented in Heiner et al. (2008a,b). Both galaxies show no clear drop in total hydrogen volume densities out to larger galactocentric radii. In the case of M 83 we were able to identify candidate PDRs out to relatively large radii. In the view of photodissociated atomic hydrogen, there is no reason to assume that individual GMC densities change further away from the galactic centre. In fact, Bigiel et al. (2010) confirm that far-UV and HI emission continue to be correlated spatially out to 3 times R_{25} even. At these distances we would expect PDRs and photodissociated HI to occur just as they would more towards the galactic centre.

We generated boxplots for M 81 and reproduced boxplots for M 83 for comparison to the M 33 results at equivalent resolution. These are shown in Figure 9. In a box-and-whisker plot, or boxplot, the boxes span the lower to upper quartiles of the data (50% of the datapoints combined), with a line indicating the median value. The so-called 'whiskers' show the range of the data (1.5 times the inner quartile range of points), with outliers plotted individually (+).

The M 81 results were recalculated to match certain parameters used in M 83 and M 33 for consistency, like the solar metallicty and the foreground extinction. A solar metallicity of 8.68 was adopted (Allende Prieto et al. 2001), and the M 81 foreground extinction was taken to be 0.63 mag, where 1.37 mag was used in Heiner et al. (2008a). As a result of this, all total hydrogen volume densities derived for M 81 used here are a factor 2 lower than calculated previously.

Finally, the results presented and summarized here are in many ways similar to those of M 101 presented by Smith et al. (2000), but cannot be compared directly to our results. They found total hydrogen volume densities in the range of 30 to 1000 cm^{-3}. They used UIT data, while newer *GALEX* data has better sensitivity and the UV flux normalization can be expected to be slightly different due to the respective UIT and *GALEX* filter function. The method that was applied to M 101 used a different way of measuring the HI column density, since averages of concentric ellipses around the central UV sources were used instead of individual HI patch measurements. While averaging the column densities is expected to yield a lower overall column densities, they did not subtract a local or global HI background level. These two differences may balance each other out. Another difference is their assumptions about an internal extinction correction, which we have chosen not to apply due to geometrical considerations (Heiner et al. 2008a).

The first observation that can be made, is that there seems to be no fundamental difference between the three galaxies. In all cases we find a range of values that does not change significantly with galactocentric radius. The lowest cloud densities that we find should not constitute an actual physical limit, since these values are either due to a large separation ρ_{HI} (where it becomes questionable whether the HI is really connected to the central UV source), or possibly pushing the method to the limits of its applicability. The largest cloud densities are a better indication, since the responsible HI patches are generally closer to the central UV source and their connection is therefore more convincing. The largest densities in M 81 are lower than those of M 33 and M 83. We already speculated in Heiner et al. (2008a) that this is consistent with the fainter levels of CO emission in M 81. In the case of M 83 they appear to be lower outside the optical disc, but this feature does not show in M 33.

4.3 Conclusions

In Heiner et al. (2009) we presented our first findings of total hydrogen volume densities in candidate PDRs in M 33 using the PDR method. We used reduced resolution results to recover the volume Schmidt law of star formation in M 33 in Heiner et al. (2010). In this paper we present the complete results of applying the PDR method to M 33. We summarize our findings as follows.

1. We presented total hydrogen volume densities of candidate PDRs in M 33 obtained with the PDR method, and compared them with those found in M 81 and M 83. These PDRs occur throughout the optical discs of these galaxies and beyond. UV emission can be matched to the presence of atomic hydrogen out to the detection limit of 21-cm images.
2. We find total hydrogen volume densities of candidate PDRs in M 33 ranging from 1 to 500 cm^{-3}.
3. The densities in candidate PDRs of M 81 and M 83 are in the same range, although the spread in the M 83 results is higher, indicating the presence of higher density GMCs in M 83. The M 33 densities go up to the same level as in M 83, although the spread is narrower. The PDR method therefore yields similar results nearby (M 33) as well as further away (M 83).
4. The cloud densities presented here at two different resolutions show that the PDR method yields consistent results that are not significantly affected by resolution effects.

ACKNOWLEDGMENTS

JSH acknowledges support by a CRAQ postdoctoral fellowship. Significant parts of this work were carried out at the Kapteyn Astronomical Institute and the Space Telescope Science Institute funded by the STScI Director's Discretionary Research Fund. Data analysis for this work was done primarily using the Groningen Image Processing System GIPSY (Ekers et al. 1973; van der Hulst et al. 1992; Vogelaar and Terlouw 2001). We thank the anonymous referee for useful comments that improved this paper.

REFERENCES

Allen, R. J.: 2004, in D. L. Block, I. Puerari, K. C. Freeman, R. Groess, and E. K. Block (eds.), *Penetrating Bars Through Masks of Cosmic Dust*, Vol. 319 of *Astrophysics and Space Science Library*, p. 731

Allen, R. J., Atherton, P. D., and Tilanus, R. P. J.: 1986, *Nature* **319**, 296

Allen, R. J., Knapen, J. H., Bohlin, R., and Stecher, T. P.: 1997, *ApJ* **487**, 171

Allende Prieto, C., Lambert, D. L., and Asplund, M.: 2001, *ApJL* **556**, L63

Bigiel, F., Leroy, A., Seibert, M., Walter, F., Blitz, L., Thilker, D., and Madore, B.: 2010, *ApJL* **720**, L31

Boulesteix, J., Courtes, G., Laval, A., Monnet, G., and Petit, H.: 1974, *A&A* **37**, 33

Braine, J., Gratier, P., Kramer, C., Xilouris, E. M., Rosolowsky, E., Buchbender, C., Boquien, M., Calzetti, D., Quintana-Lacaci, G., Tabatabaei, F., Verley, S., Israel, F., van der Tak, F., Aalto, S., Combes, F., Garcia-Burillo, S., Gonzalez, M., Henkel, C., Koribalski, B., Mookerjea, B., Roellig, M., Schuster, K. F., Relaño, M., Bertoldi, F., van der Werf, P., and Wiedner, M.: 2010, *A&A* **518**, L69+

Braun, R., Thilker, D. A., Walterbos, R. A. M., and Corbelli, E.: 2009, *ApJ* **695**, 937

Courtes, G., Petit, H., Petit, M., Sivan, J.-P., and Dodonov, S.: 1987, *A&A* **174**, 28

Ekers, R. D., Allen, R. J., and Luyten, J. R.: 1973, *A&A* **27**, 77

Engargiola, G., Plambeck, R. L., Rosolowsky, E., and Blitz, L.: 2003, *ApJS* **149**, 343

Gil de Paz, A., Boissier, S., Madore, B. F., Seibert, M., Joe, Y. H., Boselli, A., Wyder, T. K., Thilker, D., Bianchi, L., Rey, S.-C., Rich, R. M., Barlow, T. A., Conrow, T., Forster, K., Friedman, P. G., Martin, D. C., Morrissey, P., Neff, S. G., Schiminovich, D., Small, T., Donas, J., Heckman, T. M., Lee, Y.-W., Milliard, B., Szalay, A. S., and Yi, S.: 2007, *ApJS* **173**, 185

Gratier, P., Braine, J., Rodriguez-Fernandez, N. J., Schuster, K. F., Kramer, C., Xilouris, E. M., Tabatabaei, F. S., Henkel, C., Corbelli, E., Israel, F., van der Werf, P. P., Calzetti, D., Garcia-Burillo, S., Sievers, A., Combes, F., Wiklind, T., Brouillet, N., Herpin, F., Bontemps, S., Aalto, S., Koribalski, B., van der Tak, F., Wiedner, M. C., Röllig, M., and Mookerjea, B.: 2010, *A&A* **522**, A3+

Heaton, H. I.: 2009, *ApJ* **694**, 978

Heiner, J. S., Allen, R. J., Emonts, B. H. C., and van der Kruit, P. C.: 2008a, *ApJ* **673**, 798

Heiner, J. S., Allen, R. J., and van der Kruit, P. C.: 2009, *ApJ* **700**, 545

Heiner, J. S., Allen, R. J., and van der Kruit, P. C.: 2010, *ApJ* **719**, 1244

Heiner, J. S., Allen, R. J., Wong, O. I., and van der Kruit, P. C.: 2008b, *A&A* **489**, 533

Israel, F. P.: 1997, *A&A* **328**, 471

Issa, M. R., MacLaren, I., and Wolfendale, A. W.: 1990, *A&A* **236**, 237

Lagrois, D. and Joncas, G.: 2009, *ApJ* **700**, 1847

Langer, W. D., Velusamy, T., Pineda, J. L., Goldsmith, P. F., Li, D., and Yorke, H. W.: 2010, *A&A* **521**, L17+

Leroy, A., Bolatto, A., Stanimirovic, S., Mizuno, N., Israel, F., and Bot, C.: 2007, *ApJ* **658**, 1027

Leroy, A. K., Bolatto, A., Bot, C., Engelbracht, C. W., Gordon, K., Israel, F. P., Rubio, M., Sandstrom, K., and Stanimirović, S.: 2009, *ApJ* **702**, 352

Magrini, L., Stanghellini, L., Corbelli, E., Galli, D., and Villaver, E.: 2010, *A&A* **512**, A63+

Magrini, L., Vílchez, J. M., Mampaso, A., Corradi, R. L. M., and Leisy, P.: 2007, *A&A* **470**, 865

Onodera, S., Kuno, N., Tosaki, T., Kohno, K., Nakanishi, K., Sawada, T., Muraoka, K., Komugi, S., Miura, R., Kaneko, H., Hirota, A., and Kawabe, R.: 2010, *ApJL* **722**, L127

Rosolowsky, E., Engargiola, G., Plambeck, R., and Blitz, L.: 2003, *ApJ* **599**, 258

Rosolowsky, E., Keto, E., Matsushita, S., and Willner, S. P.: 2007, *ApJ* **661**, 830

Rosolowsky, E. and Simon, J. D.: 2008, *ApJ* **675**, 1213

Saha, A., Thim, F., Tammann, G. A., Reindl, B., and Sandage, A.: 2006, *ApJS* **165**, 108

Schlegel, D. J., Finkbeiner, D. P., and Davis, M.: 1998, *ApJ* **500**, 525

Smith, D. A., Allen, R. J., Bohlin, R. C., Nicholson, N., and Stecher, T. P.: 2000, *ApJ* **538**, 608

Sternberg, A.: 1988, *ApJ* **332**, 400

van der Hulst, J. M., Terlouw, J. P., Begeman, K. G., Zwitser, W., and Roelfsema, P. R.: 1992, in D. M. Worrall, C. Biemesderfer, and J. Barnes (eds.), *Astronomical Data Analysis Software and Systems I*, Vol. 25 of *Astronomical Society of the Pacific Conference Series*, p. 131

van Dishoeck, E. F. and Black, J. H.: 1988, *ApJ* **334**, 771

Vila-Costas, M. B. and Edmunds, M. G.: 1992, *MNRAS* **259**, 121

Vogelaar, M. G. R. and Terlouw, J. P.: 2001, in F. R. Harnden, Jr., F. A. Primini, and H. E. Payne (eds.), *Astronomical Data Analysis Software and Systems X*, Vol. 238 of *Astronomical Society of the Pacific Conference Series*, p. 358

Wilson, C. D. and Scoville, N.: 1992, *ApJ* **385**, 512

Zaritsky, D., Elston, R., and Hill, J. M.: 1989, *AJ* **97**, 97

Online materials

Table 5.

Source no.	R.A. (2000)	DEC. (2000)	Radius (kpc)	F_{FUV}[a]	Aperture (arcsec)
1	1 33 51.371	30 38 52.01	0.23	305.35	96
2	1 33 51.052	30 41 1.18	0.40	26.08	36
3	1 33 40.271	30 35 34.72	1.16	137.22	72
4	1 34 1.540	30 37 43.83	1.27	71.03	60
5	1 34 8.658	30 39 15.42	1.63	96.25	72
6	1 33 34.135	30 33 53.24	1.71	151.01	72
7	1 33 33.401	30 41 37.88	1.88	188.70	156
8	1 33 58.709	30 34 14.98	1.92	518.50	156
9	1 34 10.340	30 46 39.52	2.06	195.81	108
10	1 34 19.129	30 44 37.26	2.35	20.08	48
11	1 33 49.897	30 29 29.97	2.84	8.61	36
12	1 33 34.036	30 47 26.00	3.16	13.63	48
13	1 34 30.170	30 40 45.20	3.40	39.95	48
14	1 34 32.634	30 47 4.24	3.47	533.69	96
15	1 33 56.051	30 27 29.73	3.66	17.29	48
16	1 34 26.824	30 53 1.06	3.87	30.87	60
17	1 34 39.056	30 44 2.28	3.97	47.50	60
18	1 34 39.500	30 50 23.27	4.19	9.20	60
19	1 33 7.349	30 42 49.34	4.36	38.62	60
20	1 33 11.217	30 23 21.93	4.55	121.16	108
21	1 34 30.256	30 57 16.33	4.84	42.43	108
22	1 33 38.929	30 20 52.34	4.99	254.41	120
23	1 34 50.221	30 54 47.24	5.32	36.57	84
24	1 34 33.331	31 0 25.62	5.60	34.03	108
25	1 33 56.608	31 0 17.50	5.71	26.68	108
26	1 34 48.391	30 58 39.46	5.77	6.93	96
27	1 32 42.053	30 24 57.91	5.90	104.96	96
28	1 34 9.835	30 21 50.99	5.95	16.44	84
29	1 34 28.980	30 25 8.31	6.33	3.97	60
30	1 34 41.170	30 28 7.71	6.55	13.20	48
31	1 32 37.749	30 40 8.36	6.62	30.09	84
32	1 34 40.370	31 4 33.49	6.68	6.86	84
33	1 35 12.068	30 46 31.11	6.72	4.99	48
34	1 34 2.713	31 5 1.82	6.88	8.76	72
35	1 32 54.210	30 50 43.38	6.99	8.58	72
36	1 32 43.372	30 15 28.60	7.09	19.50	180
37	1 34 42.536	30 25 32.17	7.25	3.86	48
38	1 33 46.842	30 13 27.45	7.30	5.01	72
39	1 34 25.430	30 19 46.10	7.46	4.12	72
40	1 34 32.897	31 9 12.91	7.72	3.12	60
41	1 33 33.651	30 8 43.02	8.29	2.09	72
42	1 34 43.114	31 12 32.42	8.63	2.69	60

[a] 10^{-15} ergs cm^{-2} s^{-1} Å^{-1}

Table 6. Locations and FUV fluxes of candidate PDRs

Source no.	ρ_{HI} (pc)	N_{HI} (10^{21} cm^{-2})	G_0	G/G_{bg}	n (cm^{-3})	[a]
1a......	121	1.91	6.53	8.01	487	0.60
1b......	161	2.02	3.67	4.51	249	0.59
1c......	403	2.17	0.59	0.72	35	0.58
2a......	40	2.11	5.02	8.18	323	0.97
2b......	202	2.37	0.20	0.33	10	0.61
2c......	363	1.57	0.06	0.10	6	0.52
2d......	363	2.17	0.06	0.10	4	0.58
3a......	242	1.82	0.73	0.81	67	0.54
3b......	242	1.51	0.73	0.81	89	0.51
3c......	403	1.99	0.26	0.29	21	0.55
4a......	202	1.74	0.55	0.69	54	0.54
4b......	202	2.11	0.55	0.69	40	0.57
4c......	242	2.85	0.38	0.48	16	0.64
4d......	403	2.17	0.14	0.17	9	0.56
5a......	161	1.94	1.16	1.84	101	0.57
5b......	161	2.51	1.16	1.84	65	0.62
5c......	323	2.31	0.29	0.46	19	0.57
5d......	403	2.85	0.19	0.29	8	0.62
6a......	161	1.25	1.82	3.21	309	0.51
6b......	282	1.19	0.59	1.05	108	0.48
6c......	363	1.51	0.36	0.64	47	0.50
6d......	403	1.31	0.29	0.51	46	0.48
6e......	403	3.88	0.29	0.51	7	0.73
7a......	164	2.39	2.19	6.06	140	0.60
7b......	205	2.39	1.40	3.88	90	0.59
8a......	161	2.31	6.23	11.83	424	0.59
8b......	202	3.14	3.99	7.57	152	0.66
8c......	323	2.19	1.56	2.96	116	0.56
8d......	403	2.42	1.00	1.89	62	0.58
9a......	161	2.17	2.35	6.08	182	0.58
9b......	202	2.05	1.51	3.89	128	0.56
9c......	202	1.65	1.51	3.89	179	0.53
9d......	363	2.02	0.47	1.20	40	0.54
10a.....	81	0.85	0.97	2.76	291	0.59
10b.....	202	0.74	0.15	0.44	55	0.46
10c.....	282	1.71	0.08	0.23	9	0.52
11a.....	81	1.94	0.41	2.31	42	0.66
11b.....	161	1.62	0.10	0.58	14	0.54
11c.....	242	2.08	0.05	0.26	4	0.56
11d.....	323	1.65	0.03	0.14	3	0.52
11e.....	363	1.57	0.02	0.11	3	0.51
11f.....	363	1.79	0.02	0.11	2	0.53
12a.....	161	1.94	0.16	0.81	18	0.56
12b.....	202	2.17	0.10	0.52	9	0.56
12c.....	242	1.68	0.07	0.36	10	0.52
12d.....	363	2.05	0.03	0.16	3	0.54
13a.....	202	1.42	0.31	0.88	53	0.50
13b.....	242	1.54	0.21	0.61	33	0.50
13c.....	242	1.85	0.21	0.61	25	0.52
13d.....	242	1.59	0.21	0.61	32	0.50
13e.....	363	1.25	0.09	0.27	20	0.47

Table 6 (cont'd)

Source no.	$\rho_{\rm HI}$ (pc)	$N_{\rm HI}$ (10^{21} cm^{-2})	G_0	G/G_{bg}	n (cm^{-3})	[a]
13f.....	363	2.22	0.09	0.27	8	0.54
14a.....	161	3.77	6.42	12.80	214	0.70
14b.....	202	3.42	4.11	8.19	168	0.66
14c.....	282	3.68	2.10	4.18	74	0.67
14d.....	282	3.25	2.10	4.18	95	0.63
15a.....	81	2.17	0.83	3.63	79	0.66
15b.....	363	1.42	0.04	0.18	7	0.48
15c.....	363	1.68	0.04	0.18	6	0.50
16a.....	40	1.14	5.94	45.90	1460	0.91
16b.....	161	1.42	0.37	2.87	68	0.51
16c.....	323	1.39	0.09	0.72	18	0.48
16d.....	323	1.05	0.09	0.72	25	0.46
16e.....	323	1.77	0.09	0.72	12	0.51
16f.....	363	1.48	0.07	0.57	13	0.48
17a.....	161	2.17	0.57	1.46	57	0.56
18a.....	40	1.19	1.77	13.71	426	0.92
18b.....	81	1.17	0.44	3.43	109	0.61
18c.....	202	1.34	0.07	0.55	15	0.50
18d.....	242	1.22	0.05	0.38	11	0.49
18e.....	282	1.14	0.04	0.28	9	0.48
18f.....	363	1.31	0.02	0.17	5	0.48
18g.....	403	1.48	0.02	0.14	3	0.49
19a.....	161	1.91	0.46	4.44	59	0.54
19b.....	242	2.02	0.21	1.98	24	0.53
19c.....	282	2.31	0.15	1.45	14	0.54
20a.....	161	2.34	1.46	11.50	139	0.57
20b.....	161	1.91	1.46	11.50	190	0.54
20c.....	242	1.91	0.65	5.11	84	0.52
20d.....	282	2.82	0.48	3.75	33	0.58
20e.....	363	2.17	0.29	2.27	31	0.53
20f.....	363	2.85	0.29	2.27	20	0.58
21a.....	81	3.11	2.04	13.85	123	0.71
21b.....	282	1.79	0.17	1.13	25	0.50
21c.....	403	3.57	0.08	0.55	4	0.63
22a.....	121	2.54	5.44	16.64	479	0.60
22b.....	161	2.59	3.06	9.36	261	0.58
22c.....	282	3.02	1.00	3.06	65	0.59
22d.....	323	3.39	0.76	2.34	40	0.61
22e.....	323	2.45	0.76	2.34	72	0.54
23a.....	81	2.14	1.76	23.08	212	0.65
23b.....	161	2.11	0.44	5.77	54	0.54
23c.....	202	2.08	0.28	3.69	36	0.53
23d.....	282	3.05	0.14	1.88	10	0.59
24a.....	121	1.48	0.73	11.97	154	0.53
24b.....	161	1.74	0.41	6.73	69	0.52
24c.....	202	1.94	0.26	4.31	38	0.52
24d.....	323	2.02	0.10	1.68	14	0.51
24e.....	323	1.59	0.10	1.68	20	0.48
24f.....	403	1.85	0.07	1.08	10	0.49
25a.....	81	1.82	1.28	11.12	207	0.63
25b.....	202	1.51	0.21	1.78	43	0.49

Table 6 (cont'd)

Source no.	$\rho_{\rm HI}$ (pc)	$N_{\rm HI}$ (10^{21} cm^{-2})	G_0	G/G_{bg}	n (cm^{-3})	[a]
25c.....	202	1.48	0.21	1.78	44	0.49
25d.....	202	1.11	0.21	1.78	64	0.47
25e.....	363	1.59	0.06	0.55	12	0.48
25f.....	403	1.68	0.05	0.44	9	0.48
25g.....	403	1.51	0.05	0.44	11	0.47
26a.....	161	1.22	0.08	1.98	23	0.51
26b.....	282	1.22	0.03	0.65	8	0.48
26c.....	323	1.28	0.02	0.49	5	0.48
26d.....	323	1.42	0.02	0.49	5	0.49
26e.....	323	1.31	0.02	0.49	5	0.49
26f.....	403	1.39	0.01	0.32	3	0.49
26g.....	403	1.37	0.01	0.32	3	0.48
27a.....	161	2.79	1.26	10.62	107	0.58
27b.....	202	2.37	0.81	6.80	90	0.54
27c.....	242	2.31	0.56	4.72	65	0.53
27d.....	282	2.62	0.41	3.47	39	0.55
27e.....	323	2.28	0.32	2.65	37	0.52
27f.....	403	2.79	0.20	1.70	17	0.55
28a.....	121	1.74	0.35	4.11	62	0.55
28b.....	202	2.05	0.13	1.48	18	0.53
28c.....	242	1.79	0.09	1.03	15	0.50
28d.....	282	2.22	0.06	0.75	8	0.52
28e.....	323	2.28	0.05	0.58	6	0.53
28f.....	323	1.99	0.05	0.58	7	0.51
29a.....	161	1.65	0.05	0.94	9	0.57
29b.....	161	1.62	0.05	0.94	10	0.57
29c.....	403	2.59	0.01	0.15	1	0.59
29d.....	403	2.02	0.01	0.15	1	0.56
30a.....	121	1.99	0.28	2.96	44	0.56
30b.....	121	1.59	0.28	2.96	61	0.54
30c.....	282	2.42	0.05	0.54	6	0.53
30d.....	363	2.05	0.03	0.33	5	0.51
31a.....	81	2.08	1.45	12.90	214	0.63
31b.....	161	1.74	0.36	3.22	69	0.51
31c.....	242	1.54	0.16	1.43	36	0.48
31d.....	242	1.79	0.16	1.43	30	0.50
31e.....	363	1.71	0.07	0.64	14	0.48
31f.....	363	2.08	0.07	0.64	11	0.50
31g.....	403	2.91	0.06	0.52	5	0.55
32a.....	161	1.54	0.08	1.80	19	0.52
32b.....	202	1.48	0.05	1.15	13	0.51
32c.....	323	1.28	0.02	0.45	6	0.48
32d.....	363	1.77	0.02	0.35	3	0.50
32e.....	363	1.97	0.02	0.35	3	0.52
32f.....	403	1.48	0.01	0.29	3	0.49
33a.....	81	1.88	0.24	3.59	42	0.65
33b.....	161	1.91	0.06	0.90	10	0.56
33c.....	202	1.82	0.04	0.57	7	0.54
33d.....	242	1.48	0.03	0.40	6	0.52
33e.....	363	2.17	0.01	0.18	2	0.54
33f.....	363	2.08	0.01	0.18	2	0.54

Table 6 (cont'd)

Source no.	$\rho_{\rm HI}$ (pc)	$N_{\rm HI}$ (10^{21} cm^{-2})	G_0	G/G_{bg}	n (cm^{-3})	[a]
33g.....	403	1.48	0.01	0.14	2	0.51
33h.....	403	1.85	0.01	0.14	2	0.53
34a.....	161	1.82	0.11	1.38	20	0.53
34b.....	202	1.85	0.07	0.88	12	0.52
34c.....	242	1.74	0.05	0.61	9	0.50
34d.....	323	1.85	0.03	0.35	5	0.50
34e.....	403	1.45	0.02	0.22	4	0.48
35a.....	121	2.34	0.18	2.71	24	0.58
35b.....	161	1.77	0.10	1.52	20	0.53
35c.....	323	1.94	0.03	0.38	4	0.51
35d.....	323	2.17	0.03	0.38	4	0.52
36a.....	121	1.48	0.42	11.38	105	0.53
36b.....	161	1.25	0.23	6.40	73	0.49
36c.....	242	2.05	0.10	2.84	17	0.51
36d.....	282	1.19	0.08	2.09	25	0.46
36e.....	323	2.05	0.06	1.60	9	0.50
36f.....	323	1.88	0.06	1.60	11	0.49
36g.....	363	1.57	0.05	1.26	11	0.47
37a.....	40	1.65	0.74	13.33	164	0.95
37b.....	242	2.17	0.02	0.37	3	0.57
37c.....	282	1.82	0.02	0.27	3	0.55
37d.....	403	1.97	0.01	0.13	1	0.55
38a.....	161	1.31	0.06	1.47	18	0.53
38b.....	242	1.22	0.03	0.65	9	0.50
38c.....	282	1.28	0.02	0.48	6	0.50
38d.....	323	0.85	0.02	0.37	8	0.48
39a.....	81	0.99	0.20	5.39	86	0.63
39b.....	121	0.99	0.09	2.40	38	0.56
39c.....	242	0.88	0.02	0.60	11	0.51
39d.....	242	0.91	0.02	0.60	11	0.51
39e.....	363	0.97	0.01	0.27	4	0.50
39f.....	363	1.14	0.01	0.27	4	0.51
39g.....	403	1.57	0.01	0.22	2	0.52
40a.....	202	1.82	0.02	0.63	5	0.59
40b.....	282	1.45	0.01	0.32	3	0.56
40c.....	323	1.54	0.01	0.25	2	0.57
40d.....	323	1.25	0.01	0.25	3	0.55
40e.....	403	1.59	0.01	0.16	1	0.56
40f.....	403	1.25	0.01	0.16	2	0.55
40g.....	403	1.28	0.01	0.16	2	0.55
41a.....	81	0.95	0.10	4.55	50	0.75
41b.....	121	0.64	0.04	2.02	35	0.69
41c.....	161	0.66	0.03	1.14	19	0.66
41d.....	282	0.64	0.01	0.37	6	0.64
41e.....	282	0.55	0.01	0.37	8	0.64
41f.....	282	0.66	0.01	0.37	6	0.64
41g.....	323	1.06	0.01	0.28	3	0.65
41h.....	403	0.98	0.004	0.18	2	0.65
42a.....	40	1.58	0.52	22.60	142	0.99
42b.....	121	1.58	0.06	2.51	16	0.64
42c.....	161	1.58	0.03	1.41	9	0.62

Table 6 (cont'd)

Source no.	ρ_{HI} (pc)	N_{HI} (10^{21} cm^{-2})	G_0	G/G_{bg}	n (cm^{-3})	[a]
42d.....	282	1.61	0.01	0.46	3	0.60
42e.....	323	1.35	0.01	0.35	3	0.59
42f.....	363	1.46	0.01	0.28	2	0.59
42g.....	363	1.12	0.01	0.28	3	0.58

[a] Fractional error

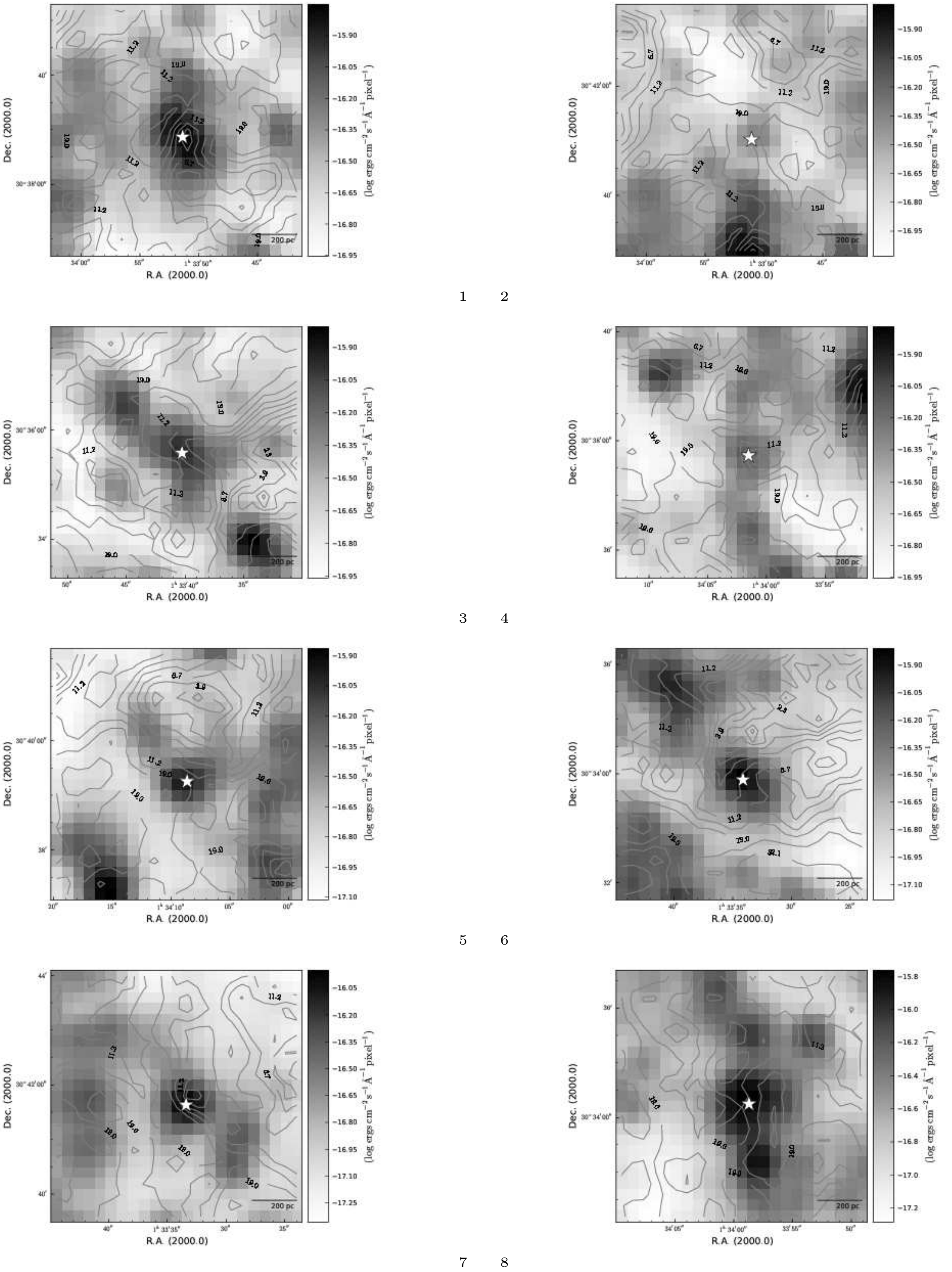

Figure 10. M33 sources 1 – 8, as described in Section 3.2 (from left to right, top to bottom). The HI column density contours are plotted against a background of the FUV flux in gray scale. The fitted position of the central UV complex is marked by a star. The integrated FUV fluxes can be found in Table 6.

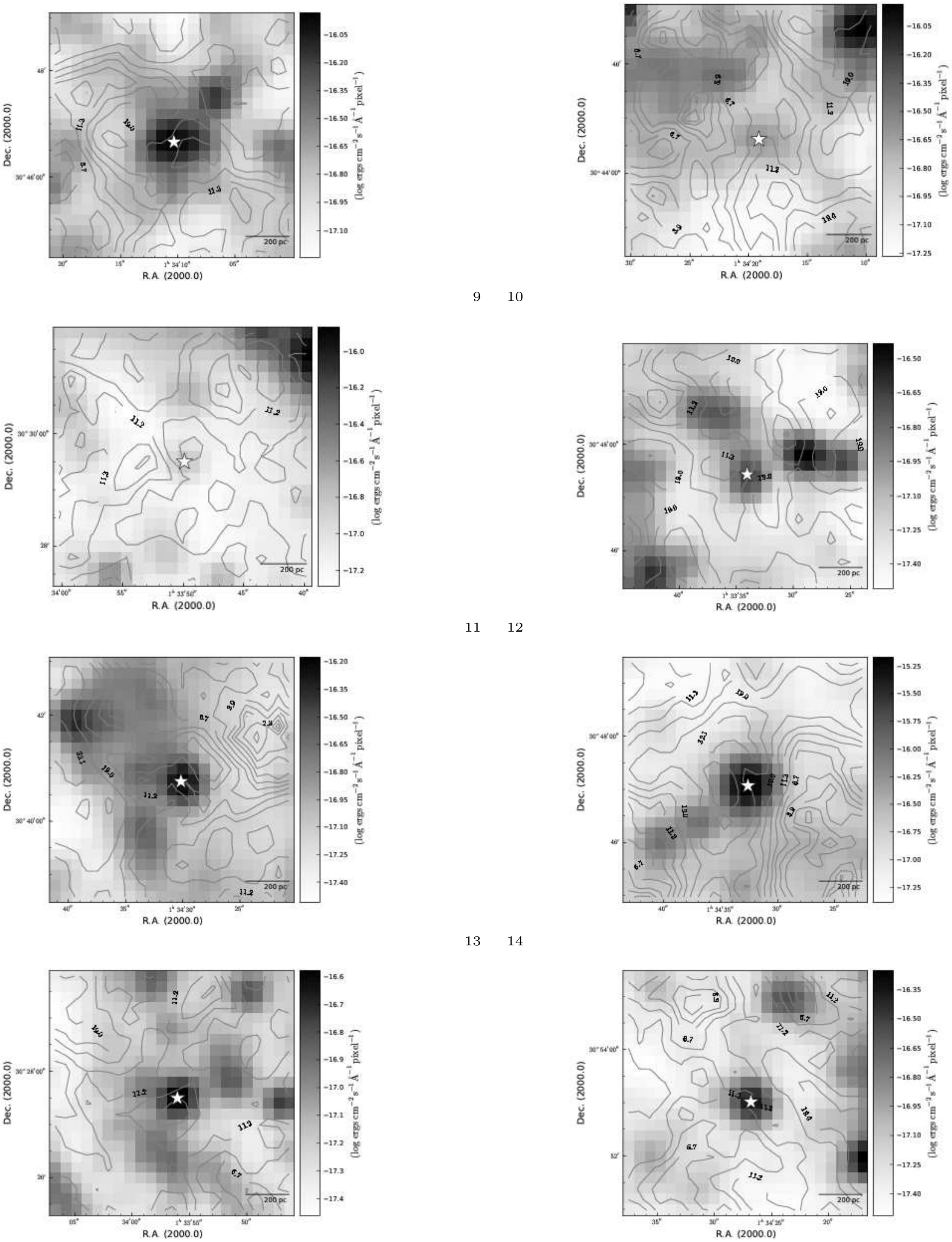

9 10

11 12

13 14

15 16

Figure 11. M33 sources 9 – 16 (from left to right, top to bottom). See Figure 10 for more details.

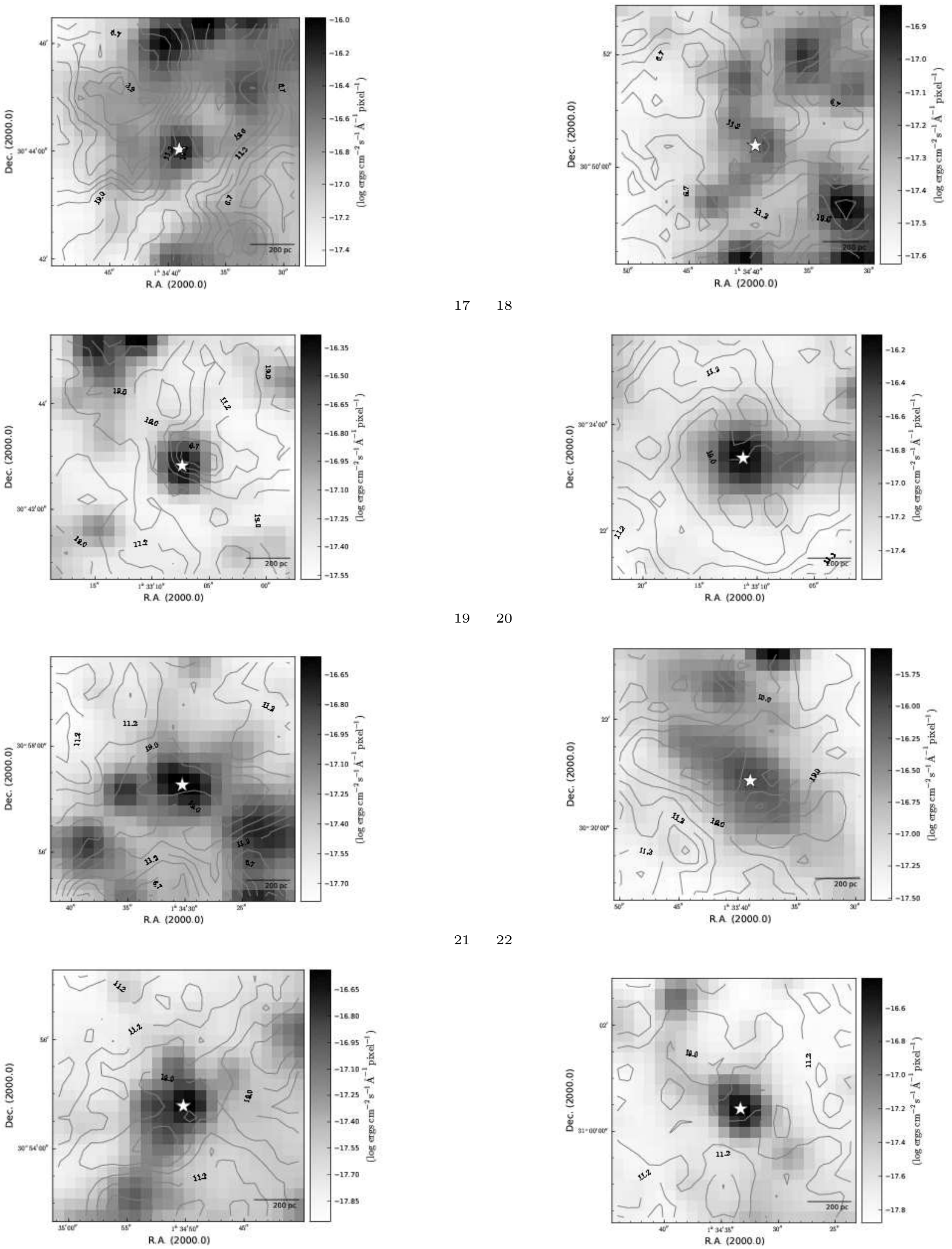

17 18

19 20

21 22

23 24

Figure 12. M33 sources 17 – 24 (from left to right, top to bottom). See Figure 10 for more details.

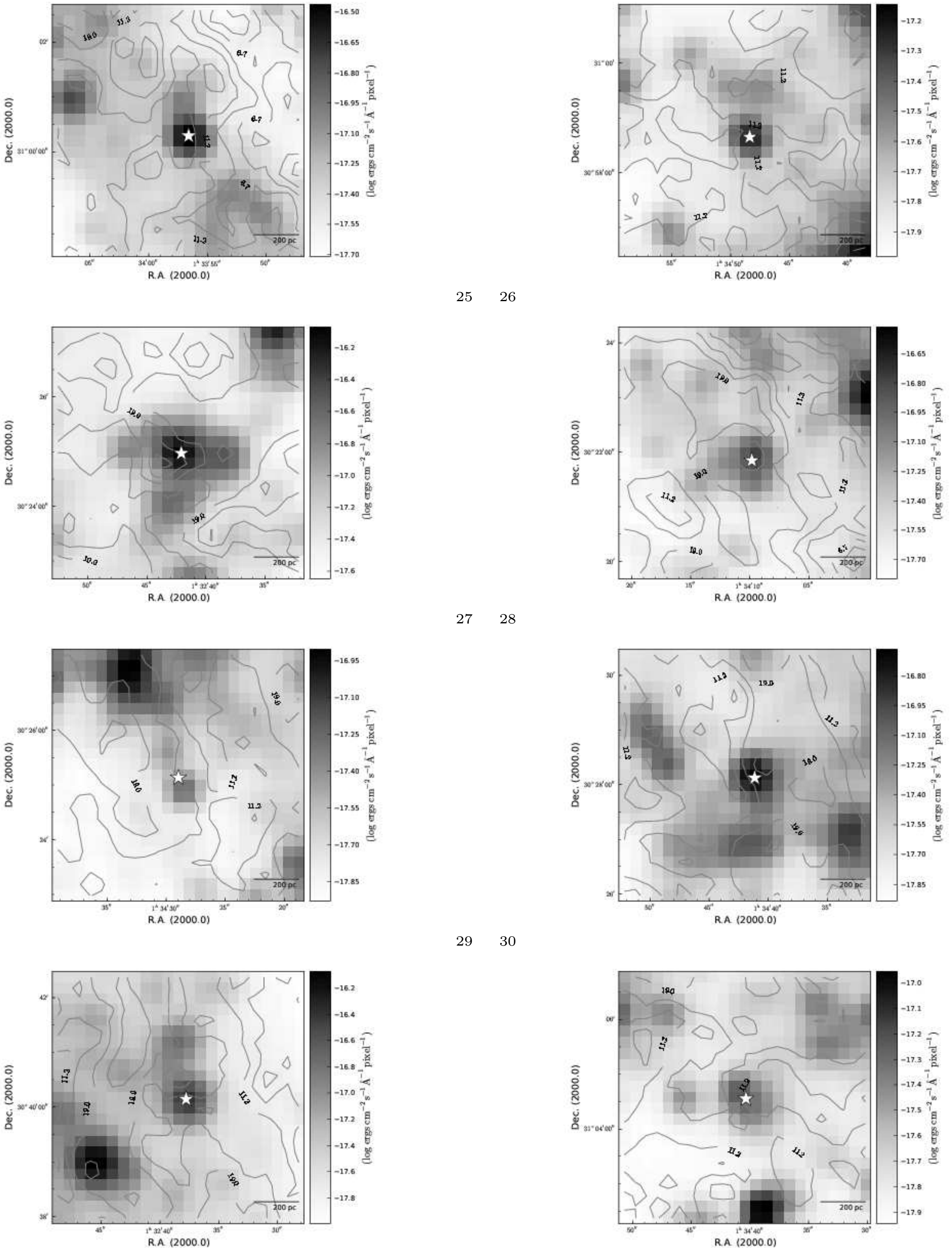

25 26

27 28

29 30

31 32

Figure 13. M33 sources 25 – 32 (from left to right, top to bottom). See Figure 10 for more details.

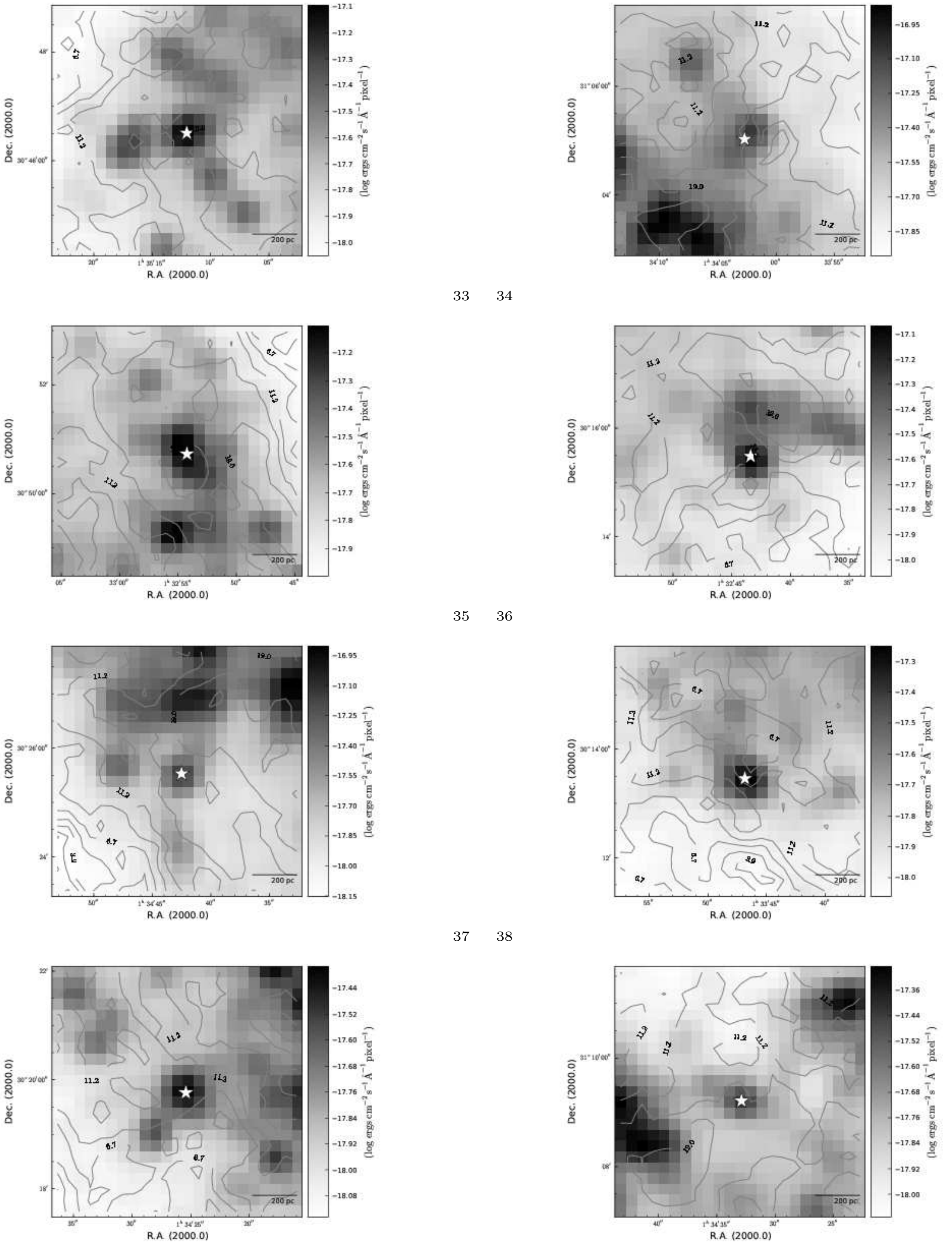

33 34

35 36

37 38

39 40

Figure 14. M33 sources 33 – 40 (from left to right, top to bottom). See Figure 10 for more details.

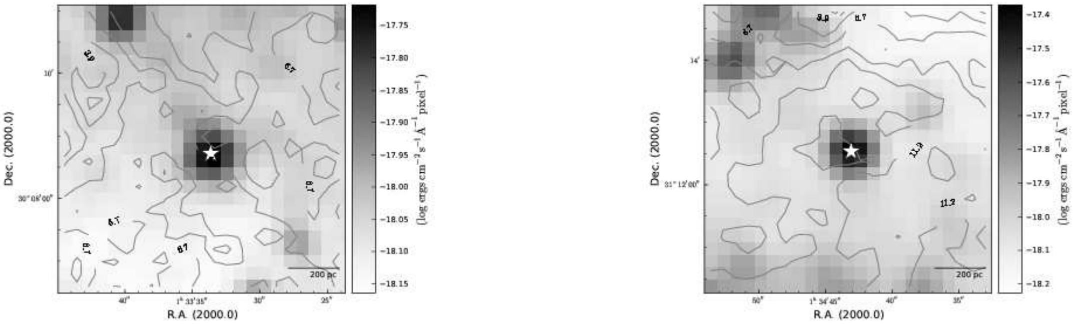

41 42

Figure 15. M33 sources 41 and 42. See Figure 10 for more details.

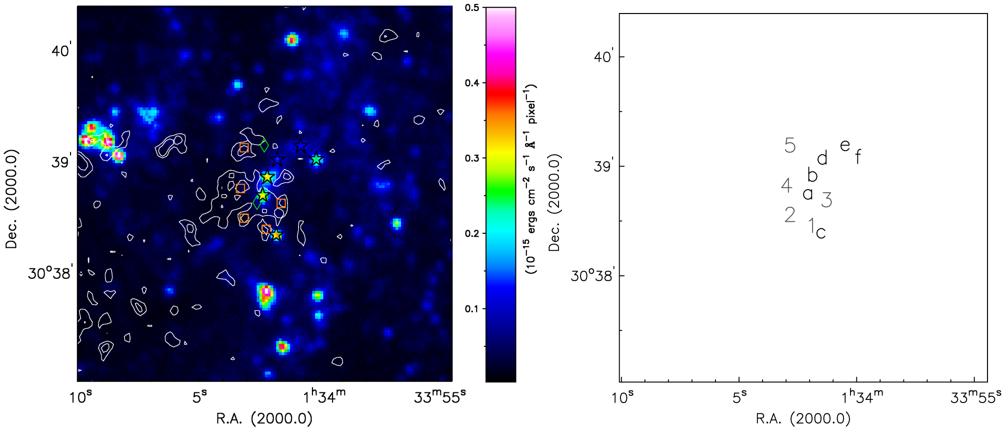

Figure 16. Left panel: CPSDP 0087g region at full resolution. The FUV color image is overlaid with HI contours. The HI contours are 3 and 4 $\times 10^{21}$cm^{-2} only, to emphasize the morphology of the HI peaks. Black stars mark the locations where the FUV fluxes were measured. The orange boxes are the locations of the measured HI patches. Green diamonds denote the location of CO detections by Engargiola et al. (2003). Part of CPSDP Z204 can be seen in the eastern part of the image. Right panel: Finding chart of the same region with letters (UV sources) and numbers (HI patches).

R_{gal} (kpc)	1.05
δ/δ_0	0.65
FUV sources (J2000)	$1^h34^m2.363^s$ $30°38'42.30''^a$, $1^h34^m2.175^s$ $30°38'52.13''^b$, $1^h34^m1.792^s$ $30°38'20.99''^c$, $1^h34^m1.754^s$ $30°39'01.48''^d$, $1^h34^m0.781^s$ $30°39'08.93''^e$, $1^h34^m0.127^s$ $30°39'01.85''^f$
FUV fluxes (10^{-15} ergs cm^{-2} s^{-1} Å^{-1})	4.55^a, 4.68^b, 4.55^c, 1.56^d, 1.65^e, 4.72^f
$N_{bg}(10^{21}$ cm$^{-2})$	0.96
$N_{HI}(10^{21}$ cm$^{-2})$	$3.37^{1:abcd}$, $4.10^{2:abc}$, $3.67^{3:abcdef}$, $4.63^{4:abcd}$, $3.64^{5:abcd}$
G_0 (cumulative)	1.69^1, 0.32^2, 0.97^3, 0.48^4, 0.37^5
G/G_{bg} range	$0.01-1.77^1$, $0.03-0.17^2$, $0.01-0.23^3$, $0.01-0.16^4$, $0.02-0.09^5$
n (derived, in cm^{-3})	15^1, 1^2, 6^3, 1^4, 3^5
Fractional error range	$0.35-0.45$

Table 7. Detailed measurements of CPSDP 0087g

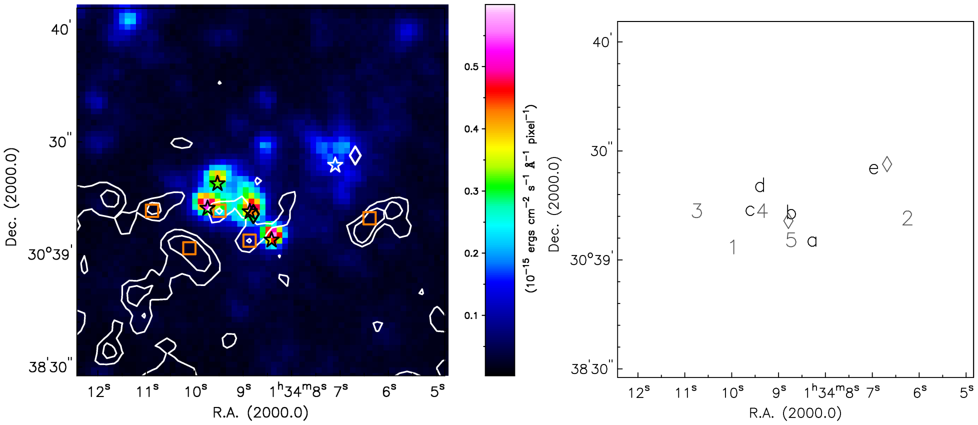

Figure 17. Left panel: CPSDP Z204 region at full resolution. The FUV color image is overlaid with HI contours. The HI contours are 3 and 4 $\times 10^{21}\mathrm{cm}^{-2}$ only, to emphasize the morphology of the HI peaks. Black stars mark the locations where the FUV fluxes were measured. The orange boxes are the locations of the measured HI patches. Diamonds denote the location of CO detections by Engargiola et al. (2003). Right panel: Finding chart of the same region with letters (UV sources) and numbers (HI patches), as well as the CO detection diamonds.

R_{gal} (kpc)	1.63
δ/δ_0	0.38
FUV sources (J2000)	$1^h34^m8.422^s$ $30°39'03.93''^a$, $1^h34^m8.874^s$ $30°39'11.48''^b$, $1^h34^m9.746^s$ $30°39'12.35''^c$, $1^h34^m9.543^s$ $30°39'18.92''^d$, $1^h34^m7.112^s$ $30°39'23.94''^e$
FUV fluxes (10^{-15} ergs cm^{-2} s^{-1} Å^{-1})	6.03^a, 6.73^b, 9.61^c, 3.72^d, 10.9^e
$N_{bg}(10^{21}$ cm$^{-2})$	0.96
$N_{HI}(10^{21}$ cm$^{-2})$	$4.56^{1:abcd}$, $4.41^{2:e}$, $3.58^{3:abcd}$, $3.38^{4:abcde}$, $3.22^{5:abcd}$
G_0 (cumulative)	0.87^1, 0.65^2, 0.45^3, 7.20^4, 3.97^5
G/G_{bg} range	$0.02-0.18^1$, 0.57^2, $0.01-0.09^3$, $0.13-1.65^4$, $0.05-0.51^5$
n (derived, in cm^{-3})	18^1, 15^2, 16^3, 295^4, 180^5
Fractional error range	$0.26-0.36$

Table 8. Detailed measurements of CPSDP Z204

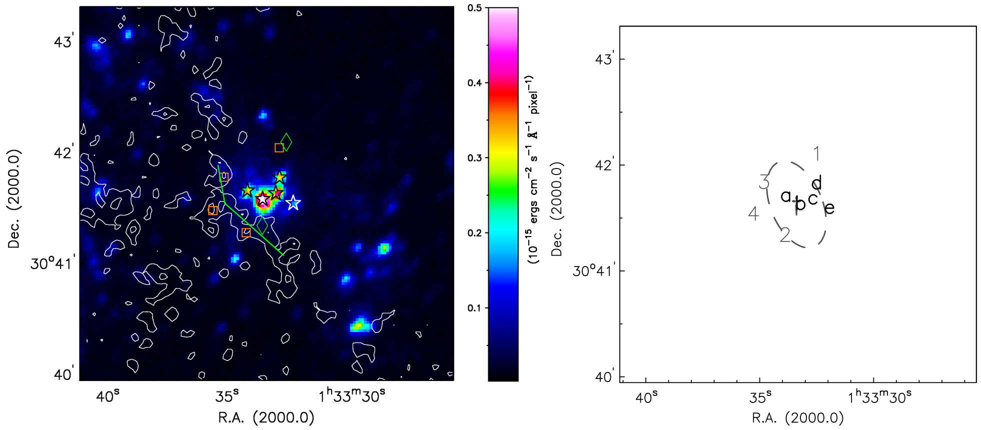

Figure 18. Left panel: NGC 595 region at full resolution. The FUV flux range is indicated in the color bar. The HI contours are 3, and 4.5×10^{21}cm^{-2}. The green line indicates the path along which the HI columns were averaged for the large scale measurement. The green diamonds mark the location of CO detections. Right panel: Finding chart of the same region with letters (UV sources) and numbers (HI patches).

R_{gal} (kpc)	1.88
δ/δ_0	0.59
FUV sources (J2000)	$1^h33^m34.134^s$ $30°41'39.68''^a$,
	$1^h33^m33.491^s$ $30°41'35.03''^b$,
	$1^h33^m32.937^s$ $30°41'38.15''^c$,
	$1^h33^m32.785^s$ $30°41'46.67''^d$,
	$1^h33^m32.208^s$ $30°41'32.86''^e$,
	$1^h33^m33.401^s$ $30°41'37.88''^{\dagger}$
FUV fluxes (10^{-15} ergs cm^{-2} s^{-1} Å^{-1})	2.75^a, 59.8^b, 4.74^c, 3.79^d, 1.76^e, $63.0^{\dagger}$
$N_{bg}(10^{21}$ cm$^{-2})$	0.93
$N_{HI}(10^{21}$ cm$^{-2})$	$1.19^{1:abcde}$, $3.79^{2:abc}$, $3.90^{3:abcd}$, $4.18^{4:ab}$, $2.48^{\dagger}$
G_0 (cumulative)	1.10^1, 1.40^2, 1.33^3, 0.54^4, $1.79^{\dagger}$
G/G_{bg} range	$0.01-1.29^1$; $0.01-2.29^2$; $0.01-2.01^3$; $0.01, 0.89^4$; $3.56^{\dagger}$
n (derived, in cm^{-3})	105^1, 12^2, 10^3, 3^4, $45^{\dagger}$
Fractional error range	0.21-0.38, $0.28^{\dagger}$

Table 9. Detailed measurements of NGC 595

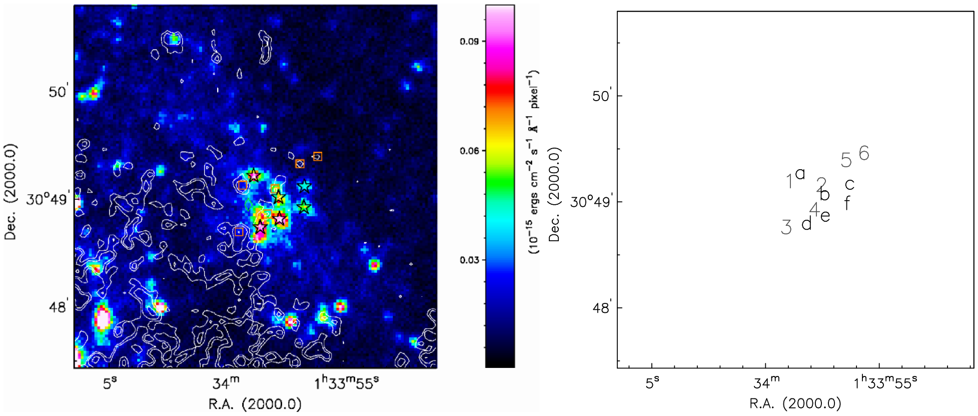

Figure 19. Same as Figure 17, but for BCLMP 0695. The Hi contours are 2, 2.5 and 3.5 $\times10^{21}$cm^{-2}. A CO detection (diamond) lies between Hi patches 1 and 4.

R_{gal} (kpc)	2.49
δ/δ_0	0.40
FUV sources (J2000)	$1^h33^m58.768^s$ $30°49'13.37''^a$, $1^h33^m57.689^s$ $30°49'01.45''^b$, $1^h33^m56.577^s$ $30°49'07.47''^c$, $1^h33^m58.480^s$ $30°48'44.72''^d$, $1^h33^m57.651^s$ $30°48'49.38''^e$, $1^h33^m56.593^s$ $30°48'55.91''^f$
FUV fluxes (10^{-15} ergs cm^{-2} s^{-1} Å^{-1})	2.26^a, 1.11^b, 0.79^c, 6.38^d, 1.73^e, 1.08^f
$N_{bg}(10^{21}$ cm$^{-2})$	0.77
$N_{HI}(10^{21}$ cm$^{-2})$	$2.60^{1:abcd}$, $1.78^{2:abcdef}$, $2.77^{3:abcd}$, $1.89^{4:abcdef}$, $1.74^{5:abcef}$, $1.46^{6:cf}$
G_0 (cumulative)	0.38^1, 1.74^2, 0.13^3, 1.14^4, 0.16^5, 0.04^6
G/G_{bg} range	$0.03-0.40^1$; $0.05-1.69^2$; $0.01-0.11^3$; $0.02-1.02^4$; $0.02-0.20^5$; $0.02, 0.06^6$
n (derived, in cm^{-3})	23^1, 195^2, 7^3, 116^4, 19^5, 5^6
Fractional error range	$0.20-0.43$

Table 10. Detailed measurements of BCLMP 0695

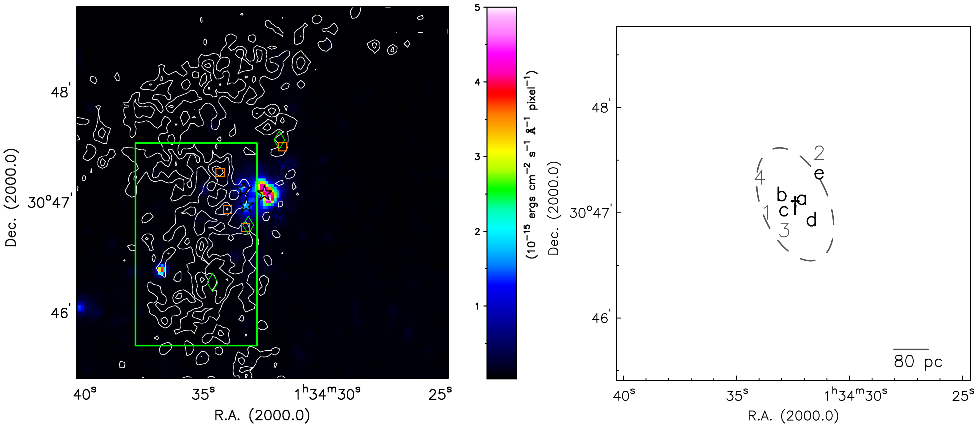

Figure 20. NGC 604 region at full resolution. The FUV flux range is indicated in the color bar. The HI contours are 3, 4 and 5 $\times 10^{21}$cm^{-2}. The green rectangle indicates the region where the HI columns were averaged for our measurement. The orange boxes are the locations of the measured HI patches. See Table 11, for the measurements corresponding to the finding chart.

R_{gal} (kpc)	3.47
δ/δ_0	0.63
FUV sources (J2000)	$1^h34^m32.42^s$ $30°47'05.2''^a$, $1^h34^m33.30^s$ $30°47'07.3''^b$, $1^h34^m33.19^s$ $30°46'58.7''^c$, $1^h34^m31.98^s$ $30°46'53.0''^d$, $1^h34^m31.64^s$ $30°47'19.9''^e$, $1^h34^m32.44^s$ $30°47'05.2''^\dagger$
FUV fluxes (10^{-15} ergs cm^{-2} s^{-1} Å^{-1})	406^a, 15.3^b, 22.6^c, 3.47^d, 8.54^e, $914^\dagger$
$N_{bg}(10^{21}$ cm$^{-2})$	0.97
$N_{HI}(10^{21}$ cm$^{-2})$	$4.19^{1:abcd}$, $2.63^{2:ade}$, $2.98^{3:abcd}$, $4.64^{4:abcd}$, $1.93^\dagger$
G_0 (cumulative)	7.40^1, 6.06^2, 10.53^3, 6.93^4, $15.21^\dagger$
G/G_{bg} range	$0.01 - 4.45^1$; $< 0.01 - 4.01^2$; $0.01 - 6.27^3$; $< 0.01 - 4.45^4$; $6.49^\dagger$
n (derived, in cm^{-3})	34^1, 109^2, 139^3, 22^4, $539^\dagger$
Fractional error range	0.30-0.44, $0.26^\dagger$

Table 11. Detailed measurements of NGC 604

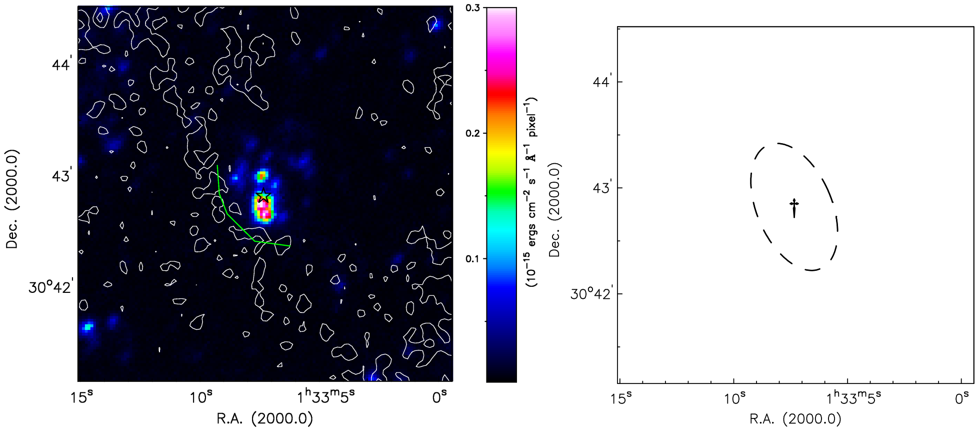

Figure 21. Same as Figure 17, but for BCLMP 0288. The HI contours are 2.5 and 4 $\times 10^{21}$cm^{-2}. This region did not show a detailed morphology, so only a large-scale measurement was made.

R_{gal} (kpc)	4.36
δ/δ_0	0.36
FUV source (J2000)	$1^h33^m07.349^s$ $30°42'49.34''$
FUV flux (10^{-15} ergs cm^{-2} s^{-1} Å^{-1})	33.2
$N_{bg}(10^{21}$ cm$^{-2})$	1.37
$N_{HI}(10^{21}$ cm$^{-2})$	1.07
G_0	0.44
G/G_{bg}	3.55
n (derived, in cm^{-3})	125
Fractional error	0.19

Table 12. Detailed measurements of BCLMP 0288

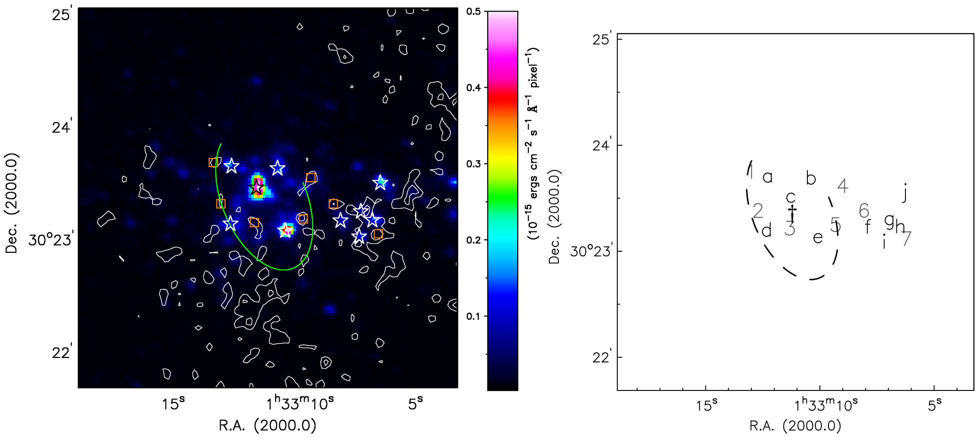

Figure 22. Same as Figure 17, but for BCLMP 0256. The HI contours are 3.5 and 4.5 $\times 10^{21}$ cm^{-2}, to reduce confusion from the presence of generous amounts of HI. The partial ellipse traces the general HI distribution peaks.

R_{gal} (kpc)	4.55
δ/δ_0	0.21^{67}, $0.22^{1235\dagger}$, 0.4^{4}
FUV sources (J2000)	$1^h33^m12.566^s$ $30°23'39.21''^a$,
	$1^h33^m10.670^s$ $30°23'38.13''^b$,
	$1^h33^m11.541^s$ $30°23'27.84''^c$,
	$1^h33^m12.608^s$ $30°23'08.57''^d$,
	$1^h33^m10.353^s$ $30°23'04.95''^e$,
	$1^h33^m08.072^s$ $30°23'10.32''^f$,
	$1^h33^m07.235^s$ $30°23'15.18''^g$,
	$1^h33^m06.760^s$ $30°23'10.58''^h$,
	$1^h33^m07.304^s$ $30°23'01.77''^i$,
	$1^h33^m06.435^s$ $30°23'30.40''^j$,
	$1^h33^m11.217^s$ $30°23'21.93''^\dagger$
FUV fluxes (10^{-15} ergs cm^{-2} s^{-1} Å^{-1})	2.58^a, 2.29^b, 16.9^c, 4.95^d, 11.0^e, 1.69^f, 0.91^g, 2.34^h, 1.36^i, 4.35^j, $61.7^\dagger$
$N_{bg}(10^{21}$ cm$^{-2})$	1.37
$N_{HI}(10^{21}$ cm$^{-2})$	$3.10^{1:acd}$, $2.54^{2:acd}$, $2.93^{3:a-e}$, $2.94^{4:befghi}$, $3.77^{5:bcefi}$, $3.21^{6:bfghij}$, $4.17^{7:f-j}$, $1.48^\dagger$
G_0 (cumulative)	0.59^1, 0.98^2, 1.25^3, 0.23^4, 0.87^5, 0.51^6, 0.97^7, $0.74^\dagger$
G/G_{bg} range	$0.11-0.38^1$; $0.10-0.92^2$, $0.02-0.53^3$, $0.01-0.15^4$, $0.03-0.86^5$, $0.02-0.73^6$, $0.08-1.26^7$, $2.30^\dagger$
n (derived, in cm^{-3})	93^1, 207^2, 217^3, 11^4, 102^5, 86^6, 109^7, $319^\dagger$
Fractional error range	$0.18-0.29$

Table 13. Detailed measurements of BCLMP 0256

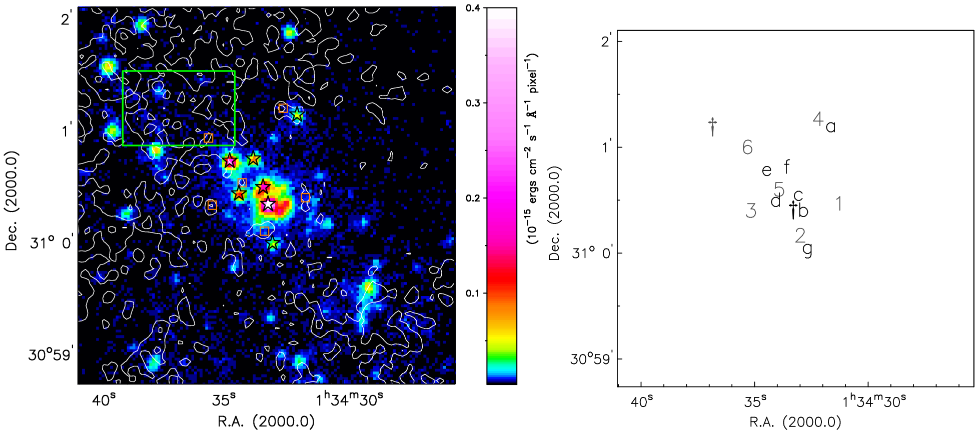

Figure 23. Same as Figure 17, but for BCLMP 0650. The HI contours are 1.5 and 2.5 $\times 10^{21}$ cm^{-2}. A global HI measurement was attempted in the rectangular region, centered on the †.

R_{gal} (kpc)	5.60
δ/δ_0	0.33
FUV sources (J2000)	$1^h34^m31.961^s$ $31°1'09.22''^a$, $1^h34^m33.158^s$ $31°0'21.19''^b$, $1^h34^m33.368^s$ $31°0'30.29''^c$, $1^h34^m34.374^s$ $31°0'26.79''^d$, $1^h34^m34.767^s$ $31°0'44.28''^e$, $1^h34^m33.785^s$ $31°0'45.55''^f$, $1^h34^m32.966^s$ $31°0'00.25''^g$, $1^h34^m33.331^s$ $31°0'25.62''^\dagger$
FUV fluxes (10^{-15} ergs cm^{-2} s^{-1} Å^{-1})	0.68^a, 5.86^b, 1.69^c, 1.11^d, 3.08^e, 0.83^f, 0.46^g, $15.7^\dagger$
$N_{bg}(10^{21}$ cm$^{-2})$	0.71
$N_{HI}(10^{21}$ cm$^{-2})$	$1.24^{1:abcfg}$, $1.77^{2:bcdefg}$, $1.91^{3:bcdeg}$, $2.24^{4:af}$, $1.14^{5:bcdefg}$, $1.99^{6:cdef}$, $1.04^\dagger$
G_0 (cumulative)	0.13^1, 0.61^2, 0.13^3, 0.1^4, 1.04^5, 0.23^6, $0.055^\dagger$
G/G_{bg} range	$0.02-0.08^1$; $0.04-1.22^2$; $0.01-0.21^3$; $0.03, 1.45^4$; $0.06-1.42^5$; $0.01-0.86^6$; $0.23^\dagger$
n (derived, in cm^{-3})	35^1, 102^2, 20^3, 12^4, 310^5, 32^6, $18^\dagger$
Fractional error range	$0.19-0.27$, $0.18^\dagger$

Table 14. Detailed measurements of BCLMP 0650

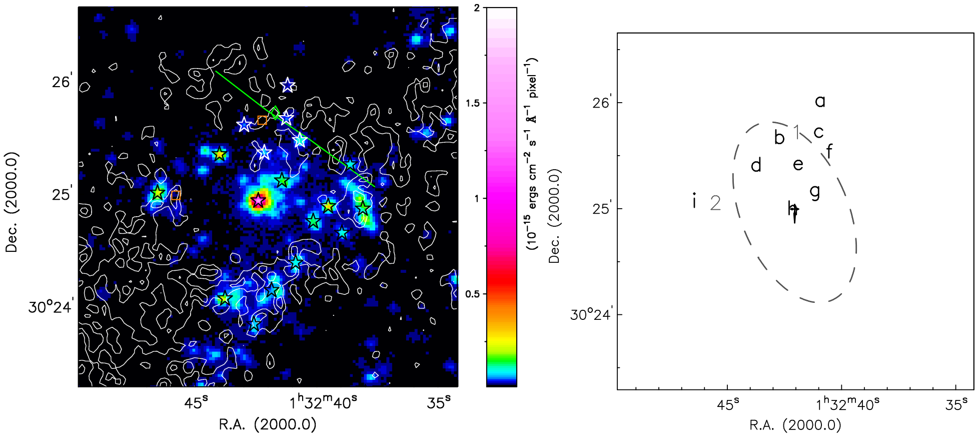

Figure 24. Same as Figure 17, but for BCLMP 0269. The HI contours are 3 and 4 $\times 10^{21}$ cm^{-2}. The right panel only contains the UV sources that were considered to be significantly impinging on the HI patches. A more global HI measurement was taken along the green line. A CO detection can also be found along this line.

R_{gal} (kpc)	5.90
δ/δ_0	0.32
FUV sources (J2000)	$1^h32^m41.199^s$ $30°25'57.90''^a$, $1^h32^m42.991^s$ $30°25'36.90''^b$, $1^h32^m41.256^s$ $30°25'40.42''^c$, $1^h32^m44.007^s$ $30°25'21.28''^d$, $1^h32^m42.159^s$ $30°25'22.11''^e$, $1^h32^m40.696^s$ $30°25'28.71''^f$, $1^h32^m41.433^s$ $30°25'07.25''^g$, $1^h32^m42.409^s$ $30°24'56.60''^h$, $1^h32^m46.560^s$ $30°25'00.72''^i$, $1^h32^m42.053^s$ $30°24'57.91''^\dagger$
FUV fluxes (10^{-15} ergs cm^{-2} s^{-1} Å^{-1})	0.24^a, 0.52^b, 0.55^c, 0.31^d, 0.56^e, 1.05^f, 1.66^g, 36.1^h, $38.2^\dagger$
$N_{bg}(10^{21}$ cm$^{-2})$	1.55
$N_{HI}(10^{21}$ cm$^{-2})$	$2.32^{1:a-h}$, $3.43^{2:i}$, $1.15^\dagger$
G_0 (cumulative)	0.42^1, 0.43^2, $0.25^\dagger$
G/G_{bg} range	$0.01 - 0.84^1$; 2.80^2, $0.87^\dagger$
n (derived, in cm^{-3})	48^1, 24^2, $77^\dagger$
Fractional error range	$0.19 - 0.26$

Table 15. Detailed measurements of BCLMP 0269

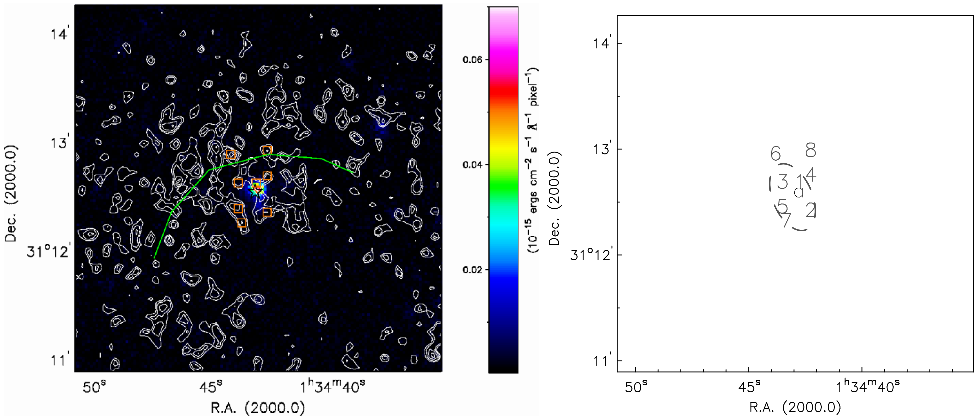

Figure 25. Our Region 42 at full resolution. Left panel: The FUV color image is overlaid with HI contours. The HI contours are 1.7, 2, 2.5, 3 and 3.5 $\times 10^{21}$cm^{-2}. The central FUV source is marked with a black star. Orange boxes mark the locations of HI patches that were measured. The green spline tracks the path along which we averaged HI column densities to get a measure of the potential large scale PDR. Right panel: Finding chart of the same region with 'a' for the UV source and numbers (HI patches). The ellipse indicates the fitted radius to the green spline in the left panel (the corresponding measurements are in *italic* in Table 16).

R_{gal}	8.63
δ/δ_0	0.27
FUV center (J2000)	$1^h34^m43.099^s$ $31^\circ12'33.25''^a$
FUV flux (10^{-15} ergs cm^{-2} s^{-1} Å^{-1})	1.44^a
$N_{bg}(10^{21}$ cm$^{-2})$	1.0
$N_{HI}(10^{21}$ cm$^{-2})$	1.49^1, 1.56^2, 1.47^3, 1.37^4. 1.73^5, 2.34^6, 1.60^7, 1.59^8, *0.51*
G_0	0.77^1, 0.14^2, 0.14^3, 0.09^4, 0.06^5, 0.04^6, 0.04^7, 0.03^8, *0.07*
G/G_{bg}	18.63^1, 3.43^2, 3.42^3, 2.07^4, 1.39^5, 0.99^6, 0.99^7, 0.66^8, *1.68*
n (derived, in cm^{-3})	227^1, 39^2, 43^3, 28^4, 14^5, 7^6, 11^7, 7^8, 71
Fractional error range	$0.19 - 0.31$, *0.21*

Table 16. Detailed measurements of Region 42